

RESEARCH ARTICLE

The microtubule-associated protein She1 coordinates directional spindle positioning by spatially restricting dynein activity

Kari H. Ecklund¹, Megan E. Bailey², Kelly A. Kossen¹, Carsten K. Dietvorst¹, Charles L. Asbury² and Steven M. Markus^{1,*}

ABSTRACT

Dynein motors move the mitotic spindle to the cell division plane in many cell types, including in budding yeast, in which dynein is assisted by numerous factors including the microtubule-associated protein (MAP) She1. Evidence suggests that She1 plays a role in polarizing dynein-mediated spindle movements toward the daughter cell; however, how She1 performs this function is unknown. We find that She1 assists dynein in maintaining the spindle in close proximity to the bud neck, such that, at anaphase onset, the chromosomes are segregated to mother and daughter cells. She1 does so by attenuating the initiation of dynein-mediated spindle movements within the mother cell, thus ensuring such movements are polarized toward the daughter cell. Our data indicate that this activity relies on She1 binding to the microtubule-bound conformation of the dynein microtubule-binding domain, and to astral microtubules within mother cells. Our findings reveal how an asymmetrically localized MAP directionally tunes dynein activity by attenuating motor activity in a spatially confined manner.

KEY WORDS: She1, Dynein, Dynactin, Microtubule-associated proteins, Spindle positioning

INTRODUCTION

By transporting various cargoes along microtubules, the dynein and kinesin families of molecular motors play important roles in many cellular processes, including coordinating the spatially and temporally appropriate positions of membrane-bound vesicles, organelles and the mitotic spindle. In addition to being affected by various motor-specific accessories and regulators, microtubule motors are regulated by a family of microtubule-associated proteins (MAPs). For instance, the neuronal MAP tau, well known for its implication in Alzheimer's disease (Iqbal et al., 2010), inhibits kinesin-1-based transport of vesicles and organelles in neurons *in vivo*, and induces detachment and pausing behavior of kinesin-1 and dynein *in vitro* (Dixit et al., 2008; Seitz et al., 2002; Tan et al., 2019; Trinczek et al., 1999). In addition to tau, several other MAPs, including MAP4 and MAP9 affect dynein transport functions *in vivo* and *in vitro* (Monroy et al., 2020; Samora et al., 2011; Semenova et al., 2014). Although the mechanisms by which MAPs affect *in vitro* motor motility are beginning to be understood

(Ecklund et al., 2017; Monroy et al., 2018, 2020; Tan et al., 2019), how their activities result in the appropriate positioning of the various dynein and kinesin cargoes in cells is unclear.

Sensitive to high expression-1 (She1) is a yeast-specific MAP that has been shown to potently affect dynein motility *in vitro* and dynein-mediated spindle positioning *in vivo* (Markus et al., 2012b, 2011; Woodruff et al., 2009). Although the precise mechanism by which She1 promotes appropriate *in vivo* dynein activity is unclear, our recent *in vitro* data determined that She1 affects dynein motility through simultaneous interactions with the dynein microtubule-binding domain (MTBD) and the microtubule (Ecklund et al., 2017). In addition to reducing dynein velocity, She1 reduces the dynein-microtubule dissociation rate (Ecklund et al., 2017), suggesting that it might promote dynein-microtubule interaction in cells and potentially affect dynein force production. Given that dynein functions in concert with the cortical receptor Num1 (potentially orthologous to NuMA in humans) (Greenberg et al., 2018; Heil-Chapdelaine et al., 2000) and the dynactin complex in cells (dynein activator) (Adames and Cooper, 2000; Geiser et al., 1997; Lee et al., 2003; Moore et al., 2008), it is unclear whether these prior findings with dynein alone apply to active Num1-dynein-dynactin complexes. Thus, a clear picture of how this MAP affects dynein-mediated spindle positioning is lacking.

She1 is one of several known effectors of budding yeast dynein activity, which also include Ndl1 (Nde1 in humans) (Li et al., 2005), Bik1 (CLIP170 in humans) (Sheeman et al., 2003) and Pac1 (LIS1 in humans) (Lee et al., 2003). In contrast to higher eukaryotes, the only known function for dynein in budding yeast is to position the nucleus with the enclosed mitotic spindle at the future site of cytokinesis (Eshel et al., 1993; Li et al., 1993), the narrow neck between the mother and daughter cells. Dynein performs this activity from cortical Num1 sites, to which it is delivered by a multi-step 'offloading' mechanism (Lee et al., 2005, 2003; Markus and Lee, 2011; Sheeman et al., 2003). Specifically, (1) dynein indirectly associates with the plus ends of dynamic microtubules in a Pac1- and Bik1-dependent manner (Lammers and Markus, 2015; Lee et al., 2003; Markus et al., 2009; Sheeman et al., 2003); (2) the dynactin complex is recruited to plus end-bound dynein (Moore et al., 2008); and (3) upon encountering cortical Num1, dynein and dynactin are offloaded and activated to translocate the nucleus and spindle (Lammers and Markus, 2015; Markus and Lee, 2011). Although the offloading process appears to be biased towards the daughter cell (Markus and Lee, 2011) – the likely result of regulated asymmetric recruitment to microtubule plus ends by Kip2, various kinases and B-type cyclins (Chen et al., 2019; Grava et al., 2006) – it is unclear whether this is sufficient to promote directionally tuned dynein activity in cells, or whether other molecules play a role in this process.

Our recent studies discovered that She1 is a key effector that polarizes dynein-mediated spindle positioning. Specifically, we

¹Department of Biochemistry and Molecular Biology, Colorado State University, Fort Collins, Colorado 80523, USA. ²Department of Physiology and Biophysics, University of Washington, Seattle, Washington 98195, USA.

*Author for correspondence (steven.markus@colostate.edu)

DOI: C.L.A., 0000-0002-0143-5394; S.M.M., 0000-0002-3098-0236

Handling Editor: David Glover

Received 8 February 2021; Accepted 27 October 2021

found that deletion of She1 compromises dynein-mediated spindle translocation events that lead to the spindle crossing the bud neck, and results in a higher prevalence of anaphase onset within the mother cells, quite distal from the bud neck (Markus et al., 2012b). How She1 performs this function, however, is unknown. In this study, we employ a combination of *in vitro* and *in vivo* methods to determine the precise basis by which She1 affects dynein activity. In particular, we find that our previous *in vitro* data indicating a role for She1 in reducing dynein velocity does not likely reflect the basis by which it reduces in-cell dynein activity. Rather, we find that She1 supports dynein-mediated spindle positioning by attenuating the initiation of cortical dynein–dynactin-mediated spindle movements predominantly in the mother cell, and that this is potentially a consequence of She1 reducing the plus end localization of dynein–dynactin complexes in this compartment. We find that this activity requires She1 interactions with the microtubule-bound conformation of the dynein microtubule-binding domain as well as microtubules, partially reconciling our *in vivo* and *in vitro* data. Although unclear, our findings suggest that She1 may affect dynein localization and activity by promoting the autoinhibited ‘phi’ conformational state of dynein. Finally, we find that the likely basis for mother cell-specific inhibition of dynein activity is the asymmetric binding of She1 to astral microtubules within this compartment. In summary, our work describes how an asymmetrically localized MAP can spatially tune the activity of a molecular motor to coordinate appropriate cargo transport.

RESULTS

She1 is required for normal spindle positioning and mitotic timing

We previously found that She1 is important for polarizing dynein-mediated spindle movements towards the daughter cell (Markus et al., 2012b). Consistent with its importance in spindle positioning, single time-point images acquired of cells grown at low temperatures (16°C; to exacerbate dynamic microtubule-mediated processes) revealed a mild spindle positioning defect (Ecklund et al., 2017). To gain additional insight into the role of She1 in dynein-mediated spindle positioning and cell cycle progression, we performed time lapse imaging of cells over the course of several cell cycles using a microfluidics-based platform (CellAsic ONIX, Millipore Sigma), in which cells are imaged at 30°C in the presence of constantly replenished nutrients. We imaged cells expressing Spc110–Venus, NLS–3mCherry and mTurquoise2–Tub1 to visualize spindle pole bodies (SPBs), the nucleus and microtubules, respectively. Consistent with the low-temperature single time-point assay (Ecklund et al., 2017), 17.7% of *she1Δ* cells (compared to only 2.5% of *SHE1* cells) exhibited mispositioned spindles at anaphase onset, confirming the importance of She1 in spindle positioning (Fig. 1A,B).

Given that She1 is important for proper spindle positioning, we wondered whether *she1Δ* cells exhibited any cell cycle delays. Cells with mispositioned spindles trigger the spindle positioning checkpoint (SPC), which delays cytokinesis and mitotic exit by preventing activation of the mitotic exit network (MEN) (Bardin et al., 2000; Bloecher et al., 2000; Caydasi et al., 2010; Daum et al., 2000; Pereira et al., 2000; Yeh et al., 1995). We assessed several aspects of cell cycle progression by measuring the time intervals between various temporal landmarks (Fig. S1). This revealed an 11.0% increase in mitotic duration in *she1Δ* cells (Fig. 1C; see Fig. S1 and Materials and Methods) that was largely a consequence of a delay between anaphase onset and cytokinesis (Fig. 1E). This is likely reflective of the previously determined dynein-independent

role for She1 in promoting spindle disassembly and thus mitotic exit (Woodruff et al., 2010). We observed no significant delay between SPB duplication and anaphase onset due to She1 deletion (Fig. 1D), suggesting that the timing of spindle assembly is unperturbed upon She1 deletion. Separate analysis of cells with mispositioned spindles and those with properly positioned spindles revealed a 13.6% delay between anaphase onset and cytokinesis in *SHE1* cells (note the very small dataset due to the low prevalence of mispositioned spindles in wild-type cells), as would be expected given the presence of an intact SPC (Fig. 1F) (Bardin et al., 2000; Bloecher et al., 2000; Daum et al., 2000; Pereira et al., 2000). Although *she1Δ* cells exhibit no such delay, the daughter-bound SPB of the mispositioned spindles in almost all such cases immediately translocated into the daughter cell following anaphase, which is sufficient to silence the SPC, and promote mitotic exit.

She1 induces a persistent force-generating dynein state *in vitro* and potentially *in vivo*

We sought to clarify the role of She1 in dynein-mediated spindle positioning. In light of our previous finding that She1 enhances dynein–microtubule binding affinity (Ecklund et al., 2017), we hypothesized that She1 promotes daughter cell-directed dynein activity by enhancing its force generation capacity (by reducing dynein–microtubule dissociation). In this model, She1 assists dynein in generating sufficient force to pull the nucleus (with an enclosed spindle) through the narrow neck (about half the width of the nucleus; see Fig. 3A,B). If true, we predicted that loss of She1 would lead to scenarios where dynein-mediated spindle movements into the neck would be more prone to failure. To determine whether this is the case, we imaged dynein-mediated spindle movements in cells arrested in a metaphase-like state (‘preanaphase’) by treatment with the DNA synthesis inhibitor hydroxyurea (HU), which permits observations of many dynein-mediated spindle movements. To ensure that all spindle movements are dynein dependent, we performed these and all similar subsequent experiments in cells deleted for *KAR9*, a key member of an actomyosin-mediated spindle orientation pathway (Markus et al., 2012a; Miller and Rose, 1998), in which preanaphase spindles exhibit an oscillatory movement along the mother–daughter axis (Yeh et al., 2000). Dynein-mediated spindle movements that were directed toward the bud neck were scored based on whether they resulted in a successful or unsuccessful crossing of the neck (Fig. 1G). Whereas 61.3% of such spindle movements resulted in a neck cross in wild-type cells, this value was reduced to 27.1% in *she1Δ* cells (Fig. 1H), lending support to an assisted force model for She1 function.

To determine whether She1 affects dynein force generation, we employed optical trapping with an artificially dimerized dynein motor domain fragment that is affected by She1 in motility assays (Ecklund et al., 2017; Markus et al., 2012b) (Fig. 2A). The motility of single dynein motor-coated beads captured in an optical trap was measured in the absence or presence of 2 or 5 nM recombinant She1–HaloTag^{TMR} (She1–TMR), concentrations that approximate cellular levels (Markus et al., 2012b). As expected, pre-stall bead velocity decreased significantly in the presence of She1–TMR (Fig. 2B,C). Although there was no appreciable change in dynein stall force in the presence of She1, we observed a 4.6-fold increase in the mean stall time (Fig. 2B,D,E), indicating that She1 induces a persistent force generating state for dynein *in vitro*.

Our results indicate that She1 may improve the ability of dynein to remain bound to microtubules in the presence of an opposing

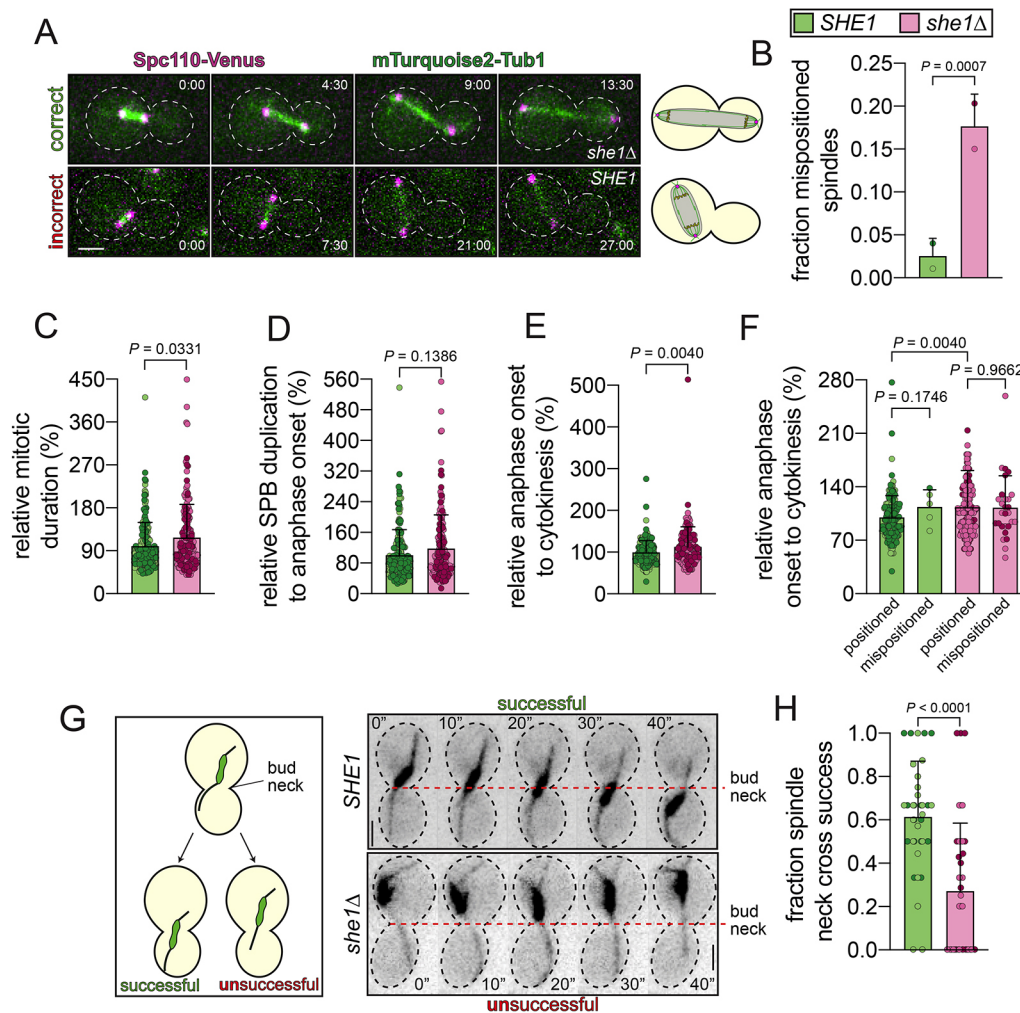


Fig. 1. She1 is required for normal spindle position and cell cycle progression. (A) Representative time-lapse images of cells expressing NLS-3mCherry (not shown here; see Fig. S1), Spc110-Venus and mTurquoise2-Tub1 depicting spindle position at the moments preceding and during anaphase onset (minutes and seconds with respect to anaphase onset are indicated). (B) Plot depicting the mean fraction (\pm s.d.) of mispositioned spindles in indicated strains (circles represent values from each independent replicate). (C–F) Plots depicting relative time intervals between various temporal landmarks (see Fig. S1; for panels B–F, $n=191$ and 163 cells from wild-type and *she1Δ*, respectively, from two independent replicates each). (G) Representative time-lapse images from HU-arrested cells expressing GFP-Tub1 depicting a successful or unsuccessful attempt of the spindle to cross the bud neck subsequent to the initiation of a dynein-mediated spindle movement toward the neck. (H) Plot depicting the fraction of bud neck-directed dynein-mediated spindle movements that result in the successful migration of the spindle midpoint across the bud neck (circles represent fraction of successful spindle neck crosses per cell; $n=40$ cells from two independent replicates for each, with $n=194$ and 146 observed spindle neck cross attempts from *SHE1* and *she1Δ* cells, respectively). *P*-values were calculated using an unpaired two-tailed Welch's *t*-test, a Mann–Whitney test, or by calculating Z score (see Materials and Methods). Dashed lines in A, G show edges of cells. Scale bars: 2 μ m.

force, which could potentially be provided by the nucleus being squeezed through the bud neck during nuclear migration. To test this *in vivo*, we employed live-cell imaging with cells expressing Nup133-3mCherry (to visualize the nucleus) and GFP-Tub1. HU-arrested cells were imaged, and we measured several parameters of dynein-mediated nuclear translocation through the bud neck, including the frequencies with which the nuclei cross the neck. Specifically, those events that were directed toward the bud neck were scored based on whether they resulted in a successful or unsuccessful insertion of the nucleus into the narrow neck (see Fig. 3C). In addition to performing this assessment in otherwise wild-type cells, we also employed cells deleted for *BNII*, a formin that when deleted results in a widening of the bud neck (Gladfelter et al., 2005; Moore et al., 2009) but not the nucleus (Fig. 3B). We reasoned that if the neck provides a barrier over which dynein-mediated nuclear migration must overcome, and that She1 assists dynein in performing this function, then widening the neck may

rescue *she1Δ* phenotypes. Although we noted a small, but statistically insignificant increase in the success rate for such events as a consequence of *BNII* deletion, the presence or absence of She1 has no apparent effect on this phenomenon (Fig. 3D). However, deletion of She1 causes a small reduction in the velocity of these movements, while combined deletion of She1 and *Bni1* increases this value to levels greater than *she1Δ* and *SHE1* cells (Fig. 3E). We also noted a small, statistically insignificant, decrease in the translocation distance in *she1Δ* cells, and a significant increase in this value for *she1Δ bni1Δ* cells (Fig. 3F), with no apparent change in the duration of these movements (Fig. 3G). These data suggest that She1 may indeed support dynein during these movements, and that widening the neck helps overcome a barrier to this translocation. However, given the lack of change in the translocation success rate, the basis by which She1 promotes dynein-mediated spindle and nuclear position remains unclear.

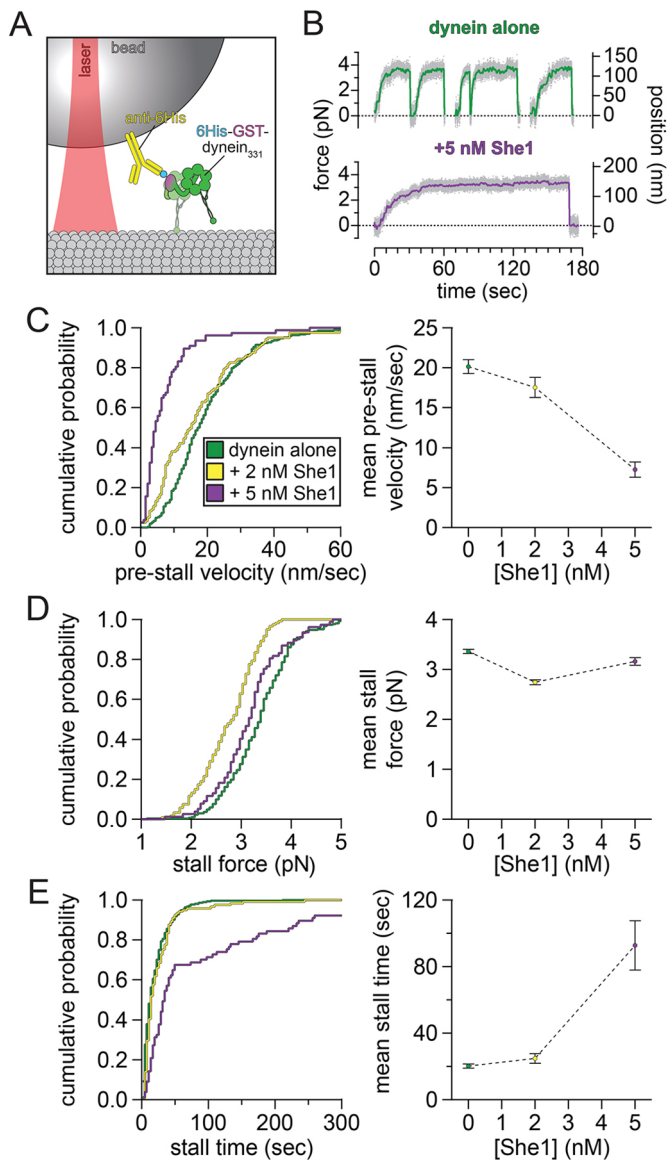


Fig. 2. She1 increases dynein stall time but not stall force. (A,B) Schematic of optical trapping experimental setup (A) and representative traces of dynein-driven bead motion in the absence or presence of She1 (B). (C–E) Plots depicting cumulative probability frequencies (left) and mean values (right; \pm s.e.m.) of pre-stall velocity (C), stall force (D) and stall time (E) for beads with single molecules of 6His–GST–dynein₃₃₁ (as determined from a microtubule-binding fraction of <0.3 ; $n=272$, 121, and 77 motility events recorded in the presence of 0, 2, and 5 nM She1-TMR, respectively).

She1 attenuates dynein activity *in vivo* and promotes bud neck proximal spindle position

Previous studies have suggested that She1 reduces dynein activity in cells (Markus et al., 2012b, 2011), which, if compartmentally specified (i.e. to the mother cell), could have the capacity to polarize dynein-mediated spindle movements (i.e. to the daughter cell). Specifically, cells lacking She1 exhibit faster and more frequent dynein-mediated spindle movements, which are apparent from spindle movements coincident with astral microtubules sliding along the cell cortex (Bergman et al., 2012; Markus et al., 2012b, 2011; Woodruff et al., 2009). We sought to determine the basis by which She1 polarizes dynein activity by performing a highly detailed assessment of dynein-mediated spindle movements. HU-arrested cells were imaged, and dynein-mediated

spindle movements were manually curated from automated spindle tracking data. We quantified various parameters of spindle movements from these data, including velocity, displacement per event and relative degree of activity (i.e. the number of events per minute, and the total dynein-mediated spindle displacement, $\text{cell}^{-1} \text{min}^{-1}$). As expected, this analysis revealed that loss of She1 led to increases in spindle velocity, displacement and overall dynein activity (Fig. 4A–E).

To gain additional insight into the role of She1 in spindle positioning, we employed a custom written code that identifies the relative position of the spindle over time with respect to the boundaries of the cells (i.e. mother versus daughter, and with respect to the bud neck or cell cortex; to account for differences in cell lengths, the lengths of all mother and daughter cells were set to 1). This revealed that loss of She1 led to: (1) the spindle spending a greater fraction of time within the mother cell, (2) an increased fraction of time during which the spindle resides within close proximity ($\leq 1 \mu\text{m}$) of the cell cortex, and (3) the spindle residing more distal from the bud neck (Fig. 4F–H). For example, whereas the spindle exhibits only a partial bias toward wild-type mother cells, with a mean position within very close proximity of the bud neck, the spindle spent a significantly larger fraction of time within *she1* Δ mother cells more distal from the neck (Fig. 4G,H).

Given previous data indicating a key role for Kar9 in polarizing the yeast microtubule network (Cepeda-García et al., 2010; Hotz et al., 2012; Liakopoulos et al., 2003; Moore et al., 2006; Pereira et al., 2001), we wanted to determine whether any of these phenotypes are a consequence of the lack of Kar9. Analysis of Kar9-expressing cells revealed a very similar pattern for all spindle position metrics noted above in *kar9* Δ cells (Fig. S2E–G), indicating that She1 polarizes dynein activity in a manner that is independent of Kar9. Interestingly, whereas She1 reduces spindle displacement values and overall dynein activity in *KAR9* cells (Fig. S2B–D) – albeit to a somewhat lesser extent – the presence of She1 had no effect on spindle velocity in these cells (Fig. S2A), indicating that this specific metric is a consequence of combined deletion of She1 and Kar9, and does not account for the polarized spindle movements promoted by She1. These observations suggest that She1 and Kar9 play complementary roles in affecting dynein motility in cells. However, given the fact that the spindle position metrics were statistically indistinguishable in *KAR9 SHE1* and *kar9* $\Delta SHE1$ cells (Fig. S2F,G; $P \geq 0.2118$), and *KAR9 she1* Δ and *kar9* $\Delta she1$ Δ cells ($P \geq 0.3557$), our results indicate that She1 polarizes dynein activity in a manner that is distinct and independent of Kar9 function.

Unlike the analyses described in Fig. 4A–E and Fig. S2A–D, which focus exclusively on dynein-dependent events, our tracking data (Fig. 4F–H and Fig. S2E–G) include all positions in which the spindle resides. To determine to what extent these positions are due to dynein, we repeated our analysis on cells deleted for the dynein heavy chain (*dyn1* Δ). As expected, these cells exhibit a large reduction in spindle movements that were only minimally increased upon further deletion of She1 (Fig. S2H). These data reveal that dynein and She1 are both required to promote spindle translocation into the daughter cell, as spindles in both *dyn1* Δ and *dyn1* $\Delta she1$ Δ cells spent a very low fraction of time in this compartment (Fig. 4G). We also noted that the spindle resides within close proximity of the cell cortex for only a small fraction of time in these mutants, indicating that this phenomenon is also dynein dependent (Fig. 4F). Finally, although deletion of *DYN1* leads to an increased distance of the spindle from the bud neck, this value was slightly increased in *dyn1* $\Delta she1$ Δ cells, suggesting that She1 may play a dynein-

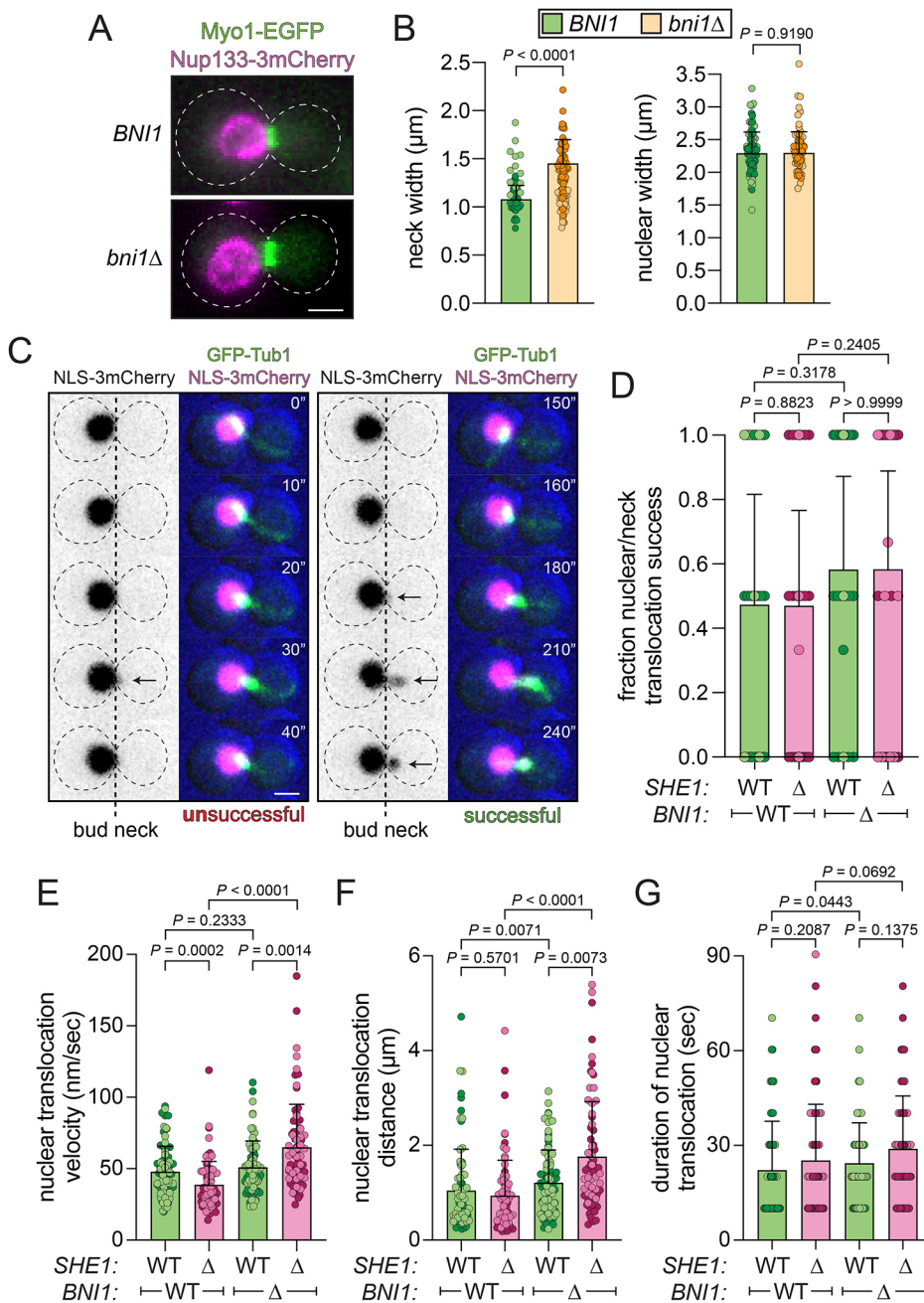


Fig. 3. She1 affects the velocity, but not the success rate, of dynein-mediated nuclear migration events through the narrow bud neck. (A,B) Representative images of HU-arrested cells expressing Nup133-3mCherry and Myo1-EFGP, and plots depicting width values of the bud neck and nucleus (\pm s.d.; $n=88$ and 67 cells, from wild-type and *bni1Δ*, respectively, from two independent replicates). (C) Example of an unsuccessful attempt to translocate the nucleus through the neck in a *BNI1* *SHE1* cell is shown on the left, and a successful attempt in the same cell is shown on the right. Arrows indicate the nucleus crossing the bud neck. (D) Plot depicting the fraction of events in which the nucleus successfully translocated the neck (\pm s.d.; circles represent success rate per cell; from left to right, $n=33$, 40, 43, and 42 cells, and 65, 74, 96, and 88 nuclear translocation attempts, from 2 independent replicates). We define a successful nuclear/neck translocation as an event in which the midpoint of the nucleus moves across the bud neck coincident with a dynein-mediated spindle movement (see Materials and Methods). (E-G) Plots depicting the mean velocity (E), translocation distance (F), and duration (G) of those events in which dynein translocates the nucleus through the bud neck (\pm s.d.; from left to right, $n=82$, 84, 83, and 77 nuclear movements, from two independent replicates). *P*-values were calculated using an unpaired two-tailed Welch's *t*-test, a Mann-Whitney test, or by calculating Z score (see Materials and Methods). Dashed lines in A, C show edges of cells. Scale bars: 2 μm.

independent role in promoting spindle/neck proximity (Fig. 4H). Taken together, these data indicate that She1 attenuates dynein-mediated spindle movements, and ensures that the spindle remains distal from the cell cortex, and within close proximity of the neck. Given the biased residence of the spindle within *she1Δ* mother cells, these data suggest that She1 may specifically reduce dynein activity within the mother cell.

She1 affects spindle position in a manner that requires its binding to cytoplasmic microtubules

Our data indicate that She1 affects at least two aspects of dynein activity: (1) the quality of dynein motility (e.g. it reduces the velocity and displacement of dynein-mediated spindle movements, although the former only in the absence of *KAR9*), and (2) initiation of dynein motility (e.g. it reduces the frequency of such events). Although our previous reconstitution experiments could potentially

account for the reduced dynein-mediated spindle velocities observed in *kar9Δ* cells, none of our *in vitro* data revealed a She1-mediated reduction in microtubule binding by dynein, raising the question of how She1 may inhibit initiation of dynein-mediated spindle translocation events. To gain insight into the mechanism underlying this phenomenon, we employed our spindle dynamics assays in combination with a series of mutants.

In addition to binding to microtubules in the cytoplasm (Woodruff et al., 2009), She1 localizes prominently to spindle microtubules in the nucleus (Wong et al., 2007), where it has been proposed to play several roles [e.g. in promoting spindle stability and disassembly, and in kinetochore function (Wong et al., 2007; Woodruff et al., 2010; Zhu et al., 2017)]. Thus, it is conceivable that loss of She1 impacts spindle movements from within the nucleus. For instance, dynein-mediated outward forces could be impacted by the loss of inward-directed forces provided by such

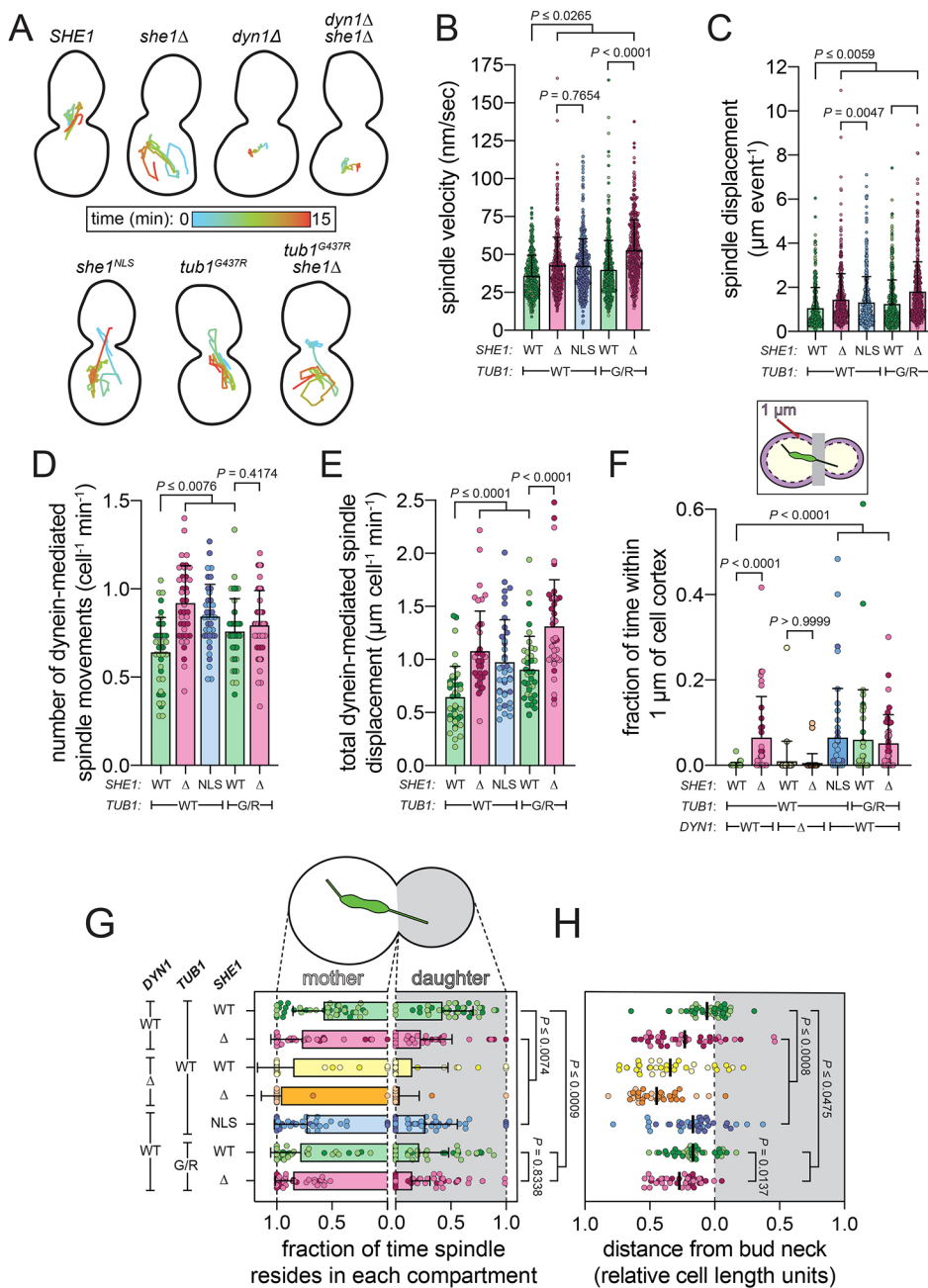


Fig. 4. Astral microtubule-bound She1 promotes bud neck proximity of the spindle and reduces dynein-mediated spindle migration events. (A) Representative spindle tracks from indicated strains. HU-arrested *kar9Δ* cells (along with indicated genotype) expressing GFP-Tub1 were imaged, and the centroid of the spindle was tracked over time. (B–E) Plots depicting (B) velocity, (C) displacement (per event), (D) and number and (E) extent (displacement per minute) of dynein-mediated spindle movements [mean \pm s.d., overlaid with all data points; from left to right, $n=315$ (40), 448 (40), 418 (38), 440 (40), and 440 (40) spindle movement events (number of cells) from two independent replicates]. (F,G) The fraction of spindle coordinates that reside within 1 μm of the cell cortex (F; mean \pm s.d. overlaid with data from individual cells) or within the mother and daughter cell are plotted (G; circles represent data for individual cells). (H) The mean longitudinal position of the spindle centroid for each cell (circles represent data for individual cells). For panels F–H, from left to right (or top to bottom for G and H) $n=40$, 40, 35, 35, 38, 40, and 40 cells from two independent replicates. For all panels, light and dark color hues indicate data points from independent replicates. G/R, *tub1*^{G437R}. *P*-values were calculated using an unpaired two-tailed Welch's *t*-test or a Mann–Whitney test (see Materials and Methods).

spindle-stabilizing factors. To determine whether it is the nuclear or cytoplasmic pool of She1 that is responsible for affecting the various spindle motility parameters, we added a strong nuclear localization signal to endogenous She1. We confirmed that She1^{NLS} is expressed at levels similar to that of wild-type She1 (Fig. S3A), is significantly enriched in the nucleus (Fig. S3B), and binds to yeast microtubules with very similar affinity to wild-type She1 (Fig. S3C–F). Of interest, we noted that the addition of the NLS eliminates the growth arrest phenotype associated with overexpressed She1 (Fig. S3G), indicating that the cytoplasmic pool – and not the nuclear pool – of She1 is causative of the sensitive-to-high-expression (*SHE*) phenotype (Espinete et al., 1995).

Analysis of spindle movements in *she1*^{NLS} cells revealed a phenotypic signature that was almost identical to that in *she1Δ* cells. This was apparent in both the quality of spindle movements

(Fig. 4A–C), the relative extent of dynein activity (Fig. 4D,E), and the spindle positioning metrics, all of which mirror that of *she1Δ* cells (Fig. 4F–H). Thus, She1 affects both the quality and quantity of dynein-mediated spindle movements from within the cytoplasm.

As noted above, our previous work demonstrated that She1 must be bound to microtubules to affect dynein motility *in vitro* (Ecklund et al., 2017). To determine whether this is the case in cells, and to assess the contribution of microtubule-bound She1 to the initiation of dynein-mediated spindle movements, we employed cells expressing a mutant α -tubulin (*Tub1*^{G437R}) to which She1 binds to a significantly reduced extent (~55.7% reduction) (Denarier et al., 2021). Consistent with the notion that She1 must bind microtubules to affect dynein motility, *tub1*^{G437R} cells exhibit increased spindle velocity and displacement values that roughly scale with the relative reduction in She1–microtubule binding in these cells (Fig. 4B,C). Moreover, *tub1*^{G437R} cells exhibit

an increase in the extent of dynein activity (Fig. 4A,D,E), mean spindle position distal from the bud neck (Fig. 4H), and increased fractions of time during which the spindle resides in close proximity of the cell cortex and within the mother cell (Fig. 4F,G). Further deletion of *She1* in *tub1^{G437R}* cells leads to more robust phenotypes, consistent with the partial ability of *She1* to bind to microtubules in these cells. We noted that some of the dynein activity metrics were higher in *tub1^{G437R} she1Δ* cells than in *TUB1 she1Δ* cells, suggesting the mutant tubulin may affect other aspects of microtubule function that impact the dynein pathway. This may be a consequence of microtubule length differences between *TUB1* and *tub1^{G437R}* cells, the latter of which exhibit a larger fraction of long microtubules (Denarier et al., 2021). Microtubule length differences have been found to correlate with increased dynein activity in cells (Estrem et al., 2017). Taken together, these data suggest that astral microtubule-bound *She1* reduces the quality and quantity of dynein-mediated spindle movements. Given the increased residence of the spindle in the mother cell in both *tub1^{G437R}* and *she1^{NLS}* cells, these data indicate that astral microtubule-bound *She1* reduces dynein activity specifically in the mother cell.

She1 does not inhibit dynein-mediated spindle movements via the dynactin microtubule-binding domain

In addition to directly impacting dynein motility, *She1* has also been implicated in affecting the interaction between dynein and dynactin, a multi-subunit complex that is required for dynein activity in cells (Markus and Lee, 2011; Markus et al., 2011; Woodruff et al., 2009). Although the mechanism by which *She1* performs this activity and the impact of this regulation on cellular dynein function are unclear, we wondered whether some of our observations are a consequence of *She1* affecting dynein–dynactin binding. Previous studies have found that human dynactin promotes a motility-competent configuration of dynein, and also stimulates microtubule-binding of the dynein–dynactin complex (McKenney et al., 2016; Zhang et al., 2017), the latter of which is due in large part to the N-terminal cytoskeleton-associated protein–glycine-rich (CAP-gly) microtubule-binding domain on the dynactin subunit p150^{Glued} (also known as DCTN1; Nip100 in budding yeast) (McKenney et al., 2016). Thus, enhanced dynein–dynactin binding could lead to an increase in the initiation of dynein-mediated spindle movements. Given that deletion of any of the dynactin subunits in yeast severely compromises dynein activity (Moore et al., 2008), we chose to employ a Nip100^{ΔCAP-gly} mutant that has been shown to have only minor effects on dynein activity (Moore et al., 2009).

With the exception of a small reduction in the time the spindle spends within the daughter cell (Fig. S4G), our analysis of *nip100^{ΔCAP-gly} kar9Δ* cells revealed no significant impact on dynein function (Fig. S4A–H). These data contrast with prior observations (Moore et al., 2009), and instead suggest that this CAP-gly domain plays a very minor role in dynein function. Moreover, additional deletion of *She1* leads to a phenotypic signature largely indistinguishable from that of *NIP100 she1Δ* cells. Although we cannot rule out the possibility that *She1* affects dynein activity in a dynactin-dependent manner, these data indicate that the dynactin MTBD is not involved in this mode of regulation.

Attenuation of dynein activity requires an interaction between She1 and a microtubule-bound dynein MTBD

We sought to determine the importance of the *She1*–dynein MTBD interaction on the various aspects of spindle migration. To this end, we employed a chimeric dynein mutant (Dyn1^{mMTBD}; in which the

MTBD is replaced by the corresponding mouse sequence) that exhibits reduced affinity for, and sensitivity to, *She1* (Ecklund et al., 2017). Given that the *dyn1^{mMTBD}* allele possesses a C-terminal 3YFP tag (in contrast to the untagged *DYN1* employed above), we compared spindle dynamics of this mutant to cells expressing Dyn1–3YFP. Although Dyn1–3YFP supports normal spindle positioning (Lee et al., 2005), we noted that these cells exhibit somewhat reduced spindle velocity values (Fig. S2A). Moreover, although deletion of *She1* led to similar alterations in most spindle migration parameters in *DYN1-3YFP* cells, many of these changes were somewhat attenuated (Fig. S2B–G), suggesting that Dyn1–3YFP is less susceptible to *She1*-mediated inhibition.

Unexpectedly, we noted a *she1Δ*-mediated increase in the quality of dynein-mediated spindle motility in *dyn1^{mMTBD}-3YFP* cells (Fig. 5A–C,F), suggesting that in-cell modulation of dynein motility by *She1* does not occur through binding to the dynein MTBD. However, the *she1Δ*-dependent increase in the extent of dynein activity in *dyn1^{mMTBD}* cells was significantly reduced compared to wild-type cells, indicating that inhibition of dynein activity by *She1* occurs in a manner that requires its interaction with the dynein MTBD (Fig. 5D,E).

Our prior *in vitro* work revealed that *She1* exhibits higher affinity for the nucleotide-free state of the dynein motor domain (Ecklund et al., 2017). Given the interaction of *She1* with the dynein MTBD, and its preferential binding to the high microtubule affinity state of the MTBD (Ecklund et al., 2017), this indicates that *She1* exhibits higher affinity for dynein when it is bound to microtubules during a processive run (Nishida et al., 2020; Uchimura et al., 2015). We also found that Dyn1^{mMTBD} exhibits a lower affinity for microtubules than the wild-type motor (Ecklund et al., 2017), suggesting that the basis for the partial insensitivity of this mutant to *She1* may be a consequence of conformational differences between the two MTBDs. To determine whether this is the case, we introduced two point mutations into Dyn1^{mMTBD} (mouse residues E3289K and E3378K, which are in the coiled-coil and MTBD, respectively) that have been reported to increase dynein–microtubule binding affinity (Redwine et al., 2012). This mutant (*dyn1^{mMTBD-HA}*, for high affinity) would be expected to spend a greater fraction of time in a microtubule-bound conformation – to which *She1* would be predicted to preferentially bind – and would potentially restore *She1* sensitivity to the chimeric mutant. Consistent with this notion, the *she1Δ*-mediated increase in the number and extent of dynein-mediated spindle movement events was completely restored in *dyn1^{mMTBD-HA} she1Δ* cells (Fig. 5D,E). Analysis of tracking data revealed an increased fraction of time during which the spindle resides within the mother cell, and a mean position more distal from the bud neck as a consequence of *She1* deletion in *dyn1^{mMTBD-HA}*, but not *dyn1^{mMTBD}* cells (Fig. 5G,H). These data indicate that *She1*-mediated inhibition of dynein activity indeed requires a microtubule-bound conformation of the MTBD. In light of the varying extents to which *She1* deletion affects the dynein activity parameters for each of the mutants, these data further support the notion that *She1*-mediated inhibition of the initiation of dynein-mediated spindle movements, and not its effect on the quality of movement, is the key determinant that dictates the ability of *She1* to promote bud neck proximity, and daughter cell-directed spindle movements.

The activity of an uninhibited dynein mutant is promoted rather than inhibited by She1

Recent data indicate that yeast dynein adopts an autoinhibited conformational state referred to as the ‘phi’ particle (Amos, 1989;

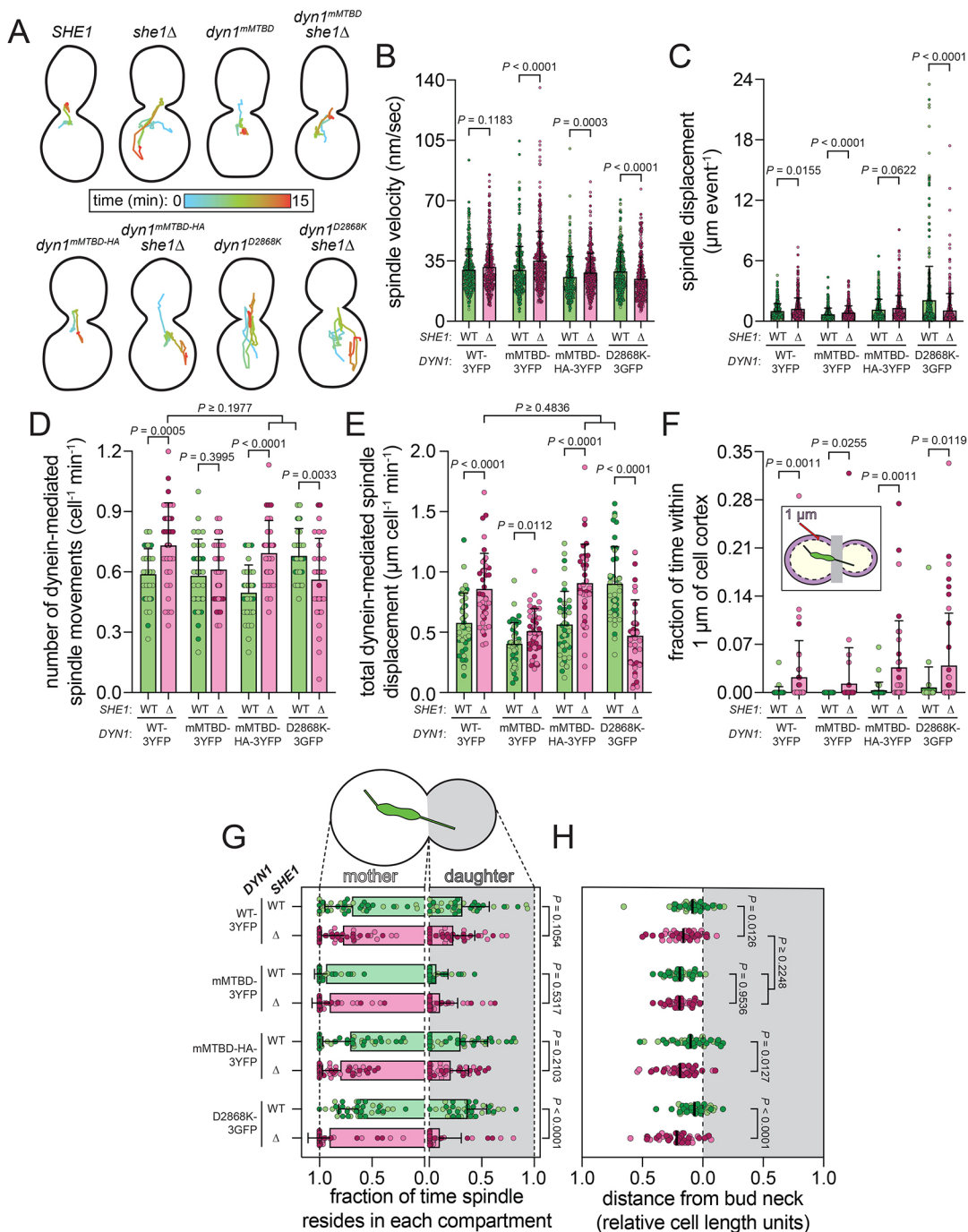


Fig. 5. She1 maintains bud neck proximity of the spindle and reduces dynein activity through interactions with the dynein MTBD. (A) Representative spindle tracks from indicated yeast strains (see Fig. 4A). (B–E) Plots depicting (B) velocity, (C) displacement (per event), (D) and number and (E) extent (displacement per minute) of dynein-mediated spindle movements [mean±s.d., overlaid with all data points; from left to right, $n=346$ (40), 418 (40), 351 (40), 361 (40), 265 (40), 417 (40), 404 (40), and 335 (40) spindle movement events (number of cells) from two independent replicates]. (F,G) The fraction of spindle coordinates that reside within 1 μm of the cell cortex (F; mean±s.d. overlaid with data from individual cells) or within the mother and daughter cell are plotted (G; circles represent data for individual cells). (H) The mean longitudinal position of the spindle centroid for each cell (circles represent data for individual cells). For panels F–H, $n=40$ cells for each from two independent replicates. For all panels, light and dark color hues indicate data points from independent replicates. WT-3YFP, *DYN1*-3YFP; mMTBD-3YFP, *dyn1^{mMTBD}*-3YFP; mMTBD-HA-3YFP, *dyn1^{mMTBD-HA}*-3YFP; D2868K-3GFP, *dyn1^{D2868K}*-3GFP. *P*-values were calculated using an unpaired two-tailed Welch's *t*-test, a Mann–Whitney test, or by calculating Z score (see Materials and Methods).

Marzo et al., 2020). This conformation restricts dynein activity in cells by precluding its interactions with cargo adaptors and dynactin (Zhang et al., 2017). Given the ability of She1 to inhibit the dynein–dynactin interaction in cells (Markus et al., 2011; Woodruff et al., 2009), we wondered whether She1 may function in part by promoting the phi conformation. To this end, we employed a dynein

mutant that is compromised in its ability to adopt this state, *Dyn1^{D2868K}* (Marzo et al., 2020). In stark contrast to all other dynein mutants tested, cells expressing *Dyn1^{D2868K}* exhibited motility and activity metrics that were reduced upon She1 deletion (Fig. 5B–E), indicating that rather than inhibit this mutant, She1 in fact promotes its activity. However, we noted that the baseline levels of activity in

dyn1^{D2868K} SHE1 cells were similar to those in *DYN1 she1Δ* cells (Fig. 5D,E), indicating that *dyn1^{D2868K}* phenocopies wild-type dynein in *she1Δ* cells.

In spite of these observations, the spindle tracking data in *dyn1^{D2868K} SHE1* and *dyn1^{D2868K} she1Δ* cells revealed a pattern very similar to cells expressing wild-type Dyn1 (Fig. 5F–H), raising the question of whether She1-mediated inhibition of the initiation of dynein-mediated spindle movements is the only determinant that dictates the ability of She1 to promote bud neck proximity and daughter cell-directed spindle movements. Moreover, these data suggest that She1 may in fact promote microtubule-binding of active cortical Num1–dynein–dynactin complexes in a manner that is reflective of our single-molecule data (Ecklund et al., 2017; Markus et al., 2012b), our optical trapping data (Fig. 2) and our nuclear/neck translocation data, in which She1 appears to support dynein-mediated translocation of the nucleus through the bud neck (Fig. 3E).

She1 inhibits the initiation of dynein-mediated spindle movements in the mother cell

We next sought to determine whether She1 directly affects the initiation of dynein-mediated spindle movements in a compartment-specific manner. Astral microtubule plus ends make contacts with the cell cortex as they dynamically sample the mother and daughter cells, with a subset of these ‘cortical contacts’ resulting in dynein-mediated spindle movements (‘productive events’; Fig. 6A). Initiation of a productive event is thought to occur coincidentally with offloading and activation of dynein–dynactin complexes at Num1 sites (Lammers and Markus, 2015; Markus and Lee, 2011). We wondered whether the increased frequency of dynein-mediated spindle movements in *she1Δ* cells is a consequence of more astral microtubule contacts with the cell cortex or more of such contacts transitioning into a productive event. To address this, we separately counted each in mother and daughter cells.

This revealed that the number of cortical contacts was significantly greater in mother than in daughter cells for almost all yeast strains (except for *dyn1^{D2868K}*; Fig. 6B), which is surprising in light of previous observations that the daughter-oriented SPB nucleates more and longer microtubules (Estrem et al., 2017; Lengfeld et al., 2018; Vogel et al., 2001; Vogel and Snyder, 2000). Although loss of She1 had very little impact on the total number of cortical contacts in most mother and daughter cells (Fig. 6B), it did cause an increase in the ratio of mother:daughter cortical contacts compared to isogenic parent strains in wild-type, *nip100^{ΔCAP-gly}* and *dyn1^{D2868K}* cells (1.27 in *SHE1* versus 1.93 in *she1Δ*; 1.91 in *nip100^{ΔCAP-gly}* versus 3.42 in *nip100^{ΔCAP-gly} she1Δ*; and, 0.98 in *dyn1^{D2868K}* versus 1.81 in *dyn1^{D2868K}*), suggesting that She1 may regulate microtubule dynamics in a compartment-specific manner, which may partially account for the mother cell bias in spindle residencies. However, this ratio was largely unchanged with respect to wild-type in *she1^{NLS}*, *tub1^{G437R}* and *tub1^{G437R} she1Δ* cells (mother:daughter ratios of 1.45, 1.35 and 1.35, respectively), indicating that relative differences in cortical contacts do not account for the mother cell bias in these mutants.

In spite of the small change in the number of microtubule-cortex encounters in *she1Δ* cells, the number of productive events was significantly greater in *she1Δ* mother, but not *she1Δ* daughter cells, compared to wild-type cells (Fig. 6C). Although the same was true for most of the other mutants that exhibit a mother cell bias of spindle residencies (i.e. *she1^{NLS}*, *tub1^{G437R} she1Δ*, *dyn1^{mMTBD-HA} she1Δ* and *dyn1^{D2868K} she1Δ*), it was not true for *tub1^{G437R}* cells, which exhibit a greater enrichment of mother cell spindle

residencies and a mean spindle position further from the neck than *she1^{NLS}* cells (see Fig. 4G,H), thus raising the question of whether the absolute number of productive events alone accounts for the spindle position phenotype. Moreover, although *dyn1^{D2868K} she1Δ* cells did not exhibit a significant increase in productive events in the mother cell, the mother:daughter ratio of these events was increased due to a reduction in events noted in the daughter cell. Unlike other mutants, this change appears to mirror the changes in cortical contacts noted as a consequence of She1 deletion, likely accounting for the mother cell bias in this mutant.

Plotting the relative fraction of cortical contacts that transition to a productive event in each compartment revealed that She1 dampens the initiation of dynein-mediated spindle migration events specifically in mother cells (Fig. 6D). Specifically, whereas an approximately equal fraction of cortical contacts in wild-type mother and daughter cells result in a productive event, these values were increased to 72.0% in *she1Δ* mother cells, but only 59.6% in *she1Δ* daughter cells. We observed a very similar pattern of disproportionate increases in the fraction of productive events in the mother cells for most of those mutants that exhibit a biased enrichment of spindle residencies in the mother cell, including *she1^{NLS}*, *tub1^{G437R}*, *tub1^{G437R} she1Δ* and *dyn1^{mMTBD-HA} she1Δ* cells. Exceptions include *nip100^{ΔCAP-gly} she1Δ* cells, which exhibited a broad distribution of values, and an overall increase in the mean activity in both mother and daughter cells upon She1 deletion (Fig. S4K), and *dyn1^{D2868K}* cells. As noted in our activity measurements described above (Fig. 5D), *dyn1^{D2868K} SHE1* cells phenocopy *DYN1 she1Δ* cells in their fraction of productive events (Fig. 6D), suggesting that preventing dynein autoinhibition renders it refractory to She1-mediated inhibition. Notably, *dyn1^{mMTBD}* cells, which exhibit no *she1Δ*-mediated shift in spindle residencies, also show no *she1Δ*-dependent increase in dynein activity in mother or daughter cells.

Taken together, these data indicate that astral microtubule-bound She1 dampens the initiation of dynein-mediated spindle movement events specifically in the mother cell in a manner that requires an interaction with the microtubule-bound conformation of the dynein MTBD. Although this activity likely accounts for the biased spindle residence in mother cells upon loss of She1, data from *nip100^{ΔCAP-gly}* and *dyn1^{D2868K}* cells raise the possibility that microtubule dynamics also plays a role in the mother cell bias. Since the probability of a dynein-mediated spindle movement is the product of the number of astral microtubule–cortical contacts and the fraction of productive events, a change in the number of cortical contacts likely affects the mean spindle position.

She1 reduces plus end localization of dynein and dynactin in the mother cell

Given that She1 reduces the likelihood of a cortical contact transitioning to a productive event specifically in the mother cell, we wondered whether She1 affects the levels of dynein or dynactin at microtubule plus ends or the cell cortex in a compartment-specific manner (Fig. 7A). Although mother and daughter *kar9Δ SHE1* cells exhibit a similar number of cortical dynein foci, this balance was shifted significantly toward mother cells in those lacking *SHE1* (Fig. 7B,C), suggesting that the increased productive events in *she1Δ* mother cells is a consequence of enhanced offloading.

Consistent with previous observations (Grava et al., 2006), we noted that daughter cells exhibit a higher frequency and intensity of plus end-associated dynein foci than mother cells, in spite of the lack of *KAR9* in these cells (Fig. 7D; $P \leq 0.0006$). We also noted a higher frequency of dynactin (Jnm1–3mCherry) at plus ends in daughter

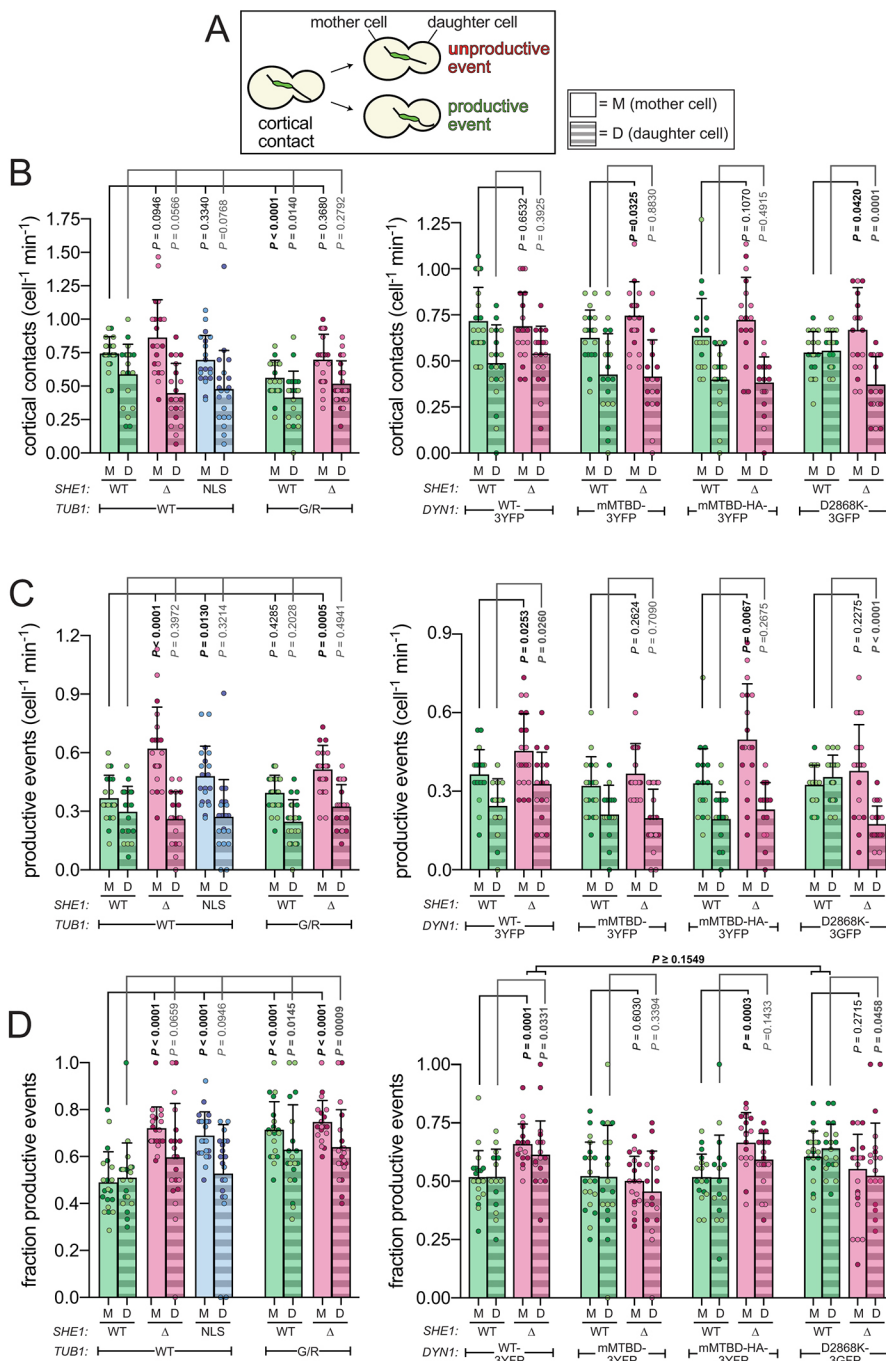


Fig. 6. She1 attenuates initiation of dynein-mediated spindle migration events in the mother cell through interactions with microtubules and the dynein MTBD. (A) Cartoon depicting events quantitated. (B–D) HU-arrested *kar9Δ* cells (along with indicated genotype) expressing GFP-Tub1 were imaged and analyzed (see Materials and Methods). (B–D) The numbers of astral microtubule plus end-cortex encounters (B) and of 'productive' dynein-mediated spindle translocation events (C) are plotted, as well as the fraction of cortical contacts that convert to a productive event (D) (mean±s.d., for all strains, *n*=20 cells from two independent replicates). For all panels, light and dark color hues indicate data points from independent replicates. *P*-values were calculated using an unpaired two-tailed Welch's *t*-test, a Mann-Whitney test, or by calculating Z score (see Materials and Methods).

than mother cells (Fig. 7E; *P*=0.0002). Interestingly, the frequency and intensity of dynein and dynactin foci were much higher in *she1Δ* mother cells (*P*<0.0001), but only slightly higher in *she1Δ* daughter cells (*P*≥0.0324), indicating that She1 precludes association of dynein and dynactin with plus ends in mother cells to a greater extent than in daughter cells. Notably, *dyn1^{MTBD} SHE1* cells exhibit levels of dynein and dynactin very similar to *DYN1 she1Δ* cells, which were only slightly increased upon deletion of *SHE1*, suggesting that She1 affects their plus end association in a manner that requires an interaction with the dynein MTBD. These data indicate that She1 may attenuate the initiation of dynein-mediated spindle movements in mother cells by preventing association of dynein and dynactin with plus ends, which in turn reduces their offloading and activation at cortical sites in this compartment.

She1 localizes preferentially to astral microtubules within the mother cell

We next wondered whether She1 preferentially localizes to astral microtubules in the mother cell. To circumvent the difficulty in visualizing endogenous levels of She1-3GFP (due to low cellular concentrations), we overexpressed She1-3GFP using the galactose-inducible promoter *GAL1p*. To correlate She1 localization patterns to our spindle dynamics data, we arrested *GAL1p:SHE1-3GFP* cells with HU. Live-cell imaging revealed a ~4-fold greater fraction of mother cells with apparent She1-3GFP along astral microtubules with respect to daughter cells (Fig. 8A,B; note only those cells with astral microtubules apparent in both compartments were assessed). Fluorescence intensity measurements confirmed its preferential localization to astral microtubules in mother cells (Fig. 8C), and that

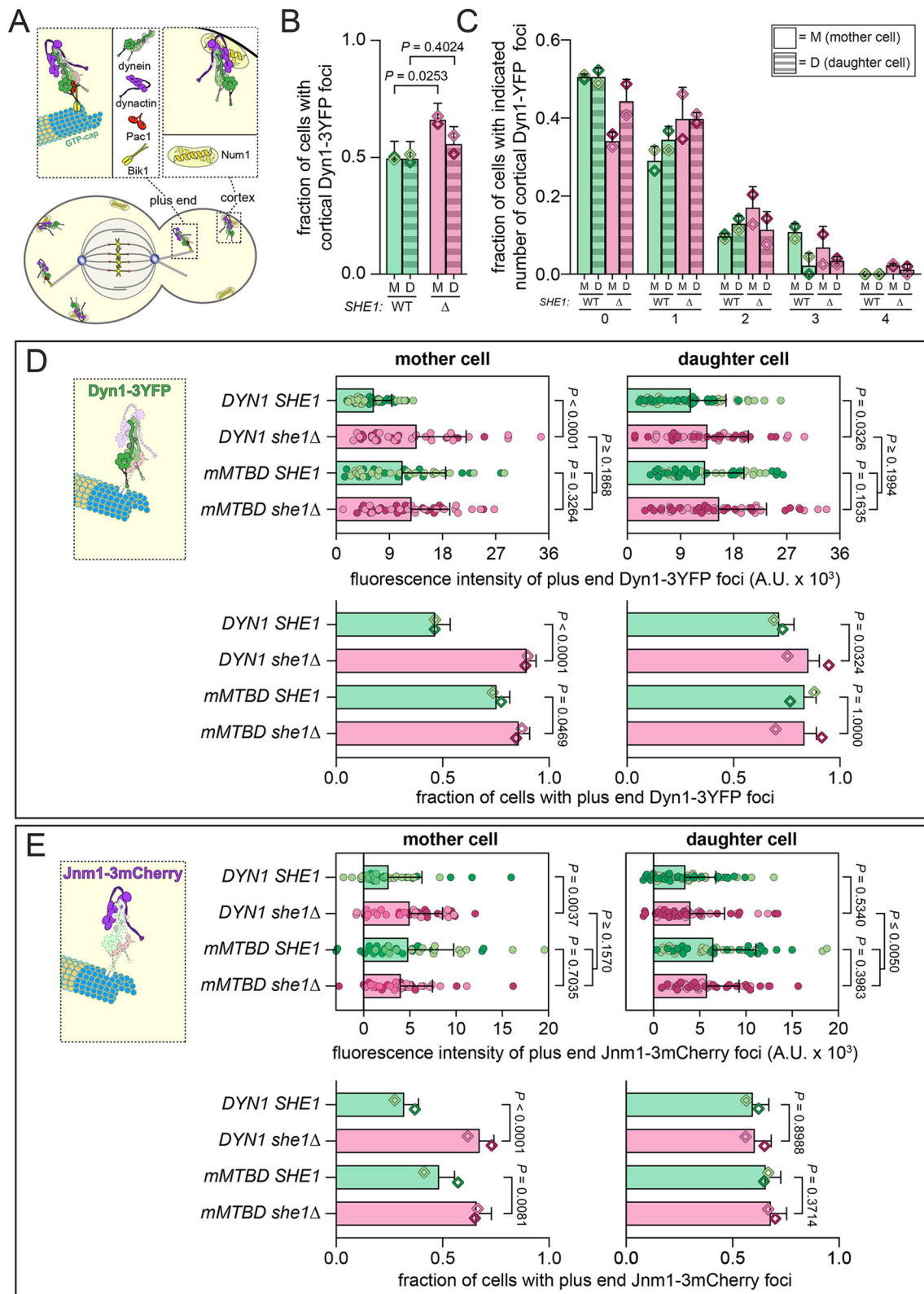


Fig. 7. She1 precludes plus end and cortical targeting of dynein and dynactin in mother cells. (A) Cartoon schematic depicting two of the sites to which dynein and dynactin localize in cells. (B,C) Plots depicting the fraction of mother (M) and daughter (D) cells with ≥ 1 cortical dynein focus (B; Dyn1-3YFP), and the fraction of cells with the indicated number of cortical Dyn1-3YFP foci per cell (C) (mean \pm standard error of proportion, $n=93$ and 88 mother and daughter cells, for *SHE1* and *she1* Δ , respectively, from two independent replicates). (D,E) Plots depicting the fluorescence intensity values of plus end-associated Dyn1-3YFP (D, top; mean \pm s.d.) or Jnm1-3mCherry foci (E, top, mean \pm s.d.), and the fraction of cells with ≥ 1 plus end foci (D and E, bottom; weighted mean \pm weighted standard error of proportion; from top to bottom, $n=39/55$, $38/47$, $40/47$ and $41/48$ Dyn1-3YFP and Jnm1-3mCherry foci (for top plots) from 97/84, 95/81, 93/90, 91/78 mother/daughter cells (for bottom plots), from two independent replicates. P -values were calculated using an unpaired two-tailed Welch's t -test, a Mann-Whitney test, or by calculating Z score (see Materials and Methods).

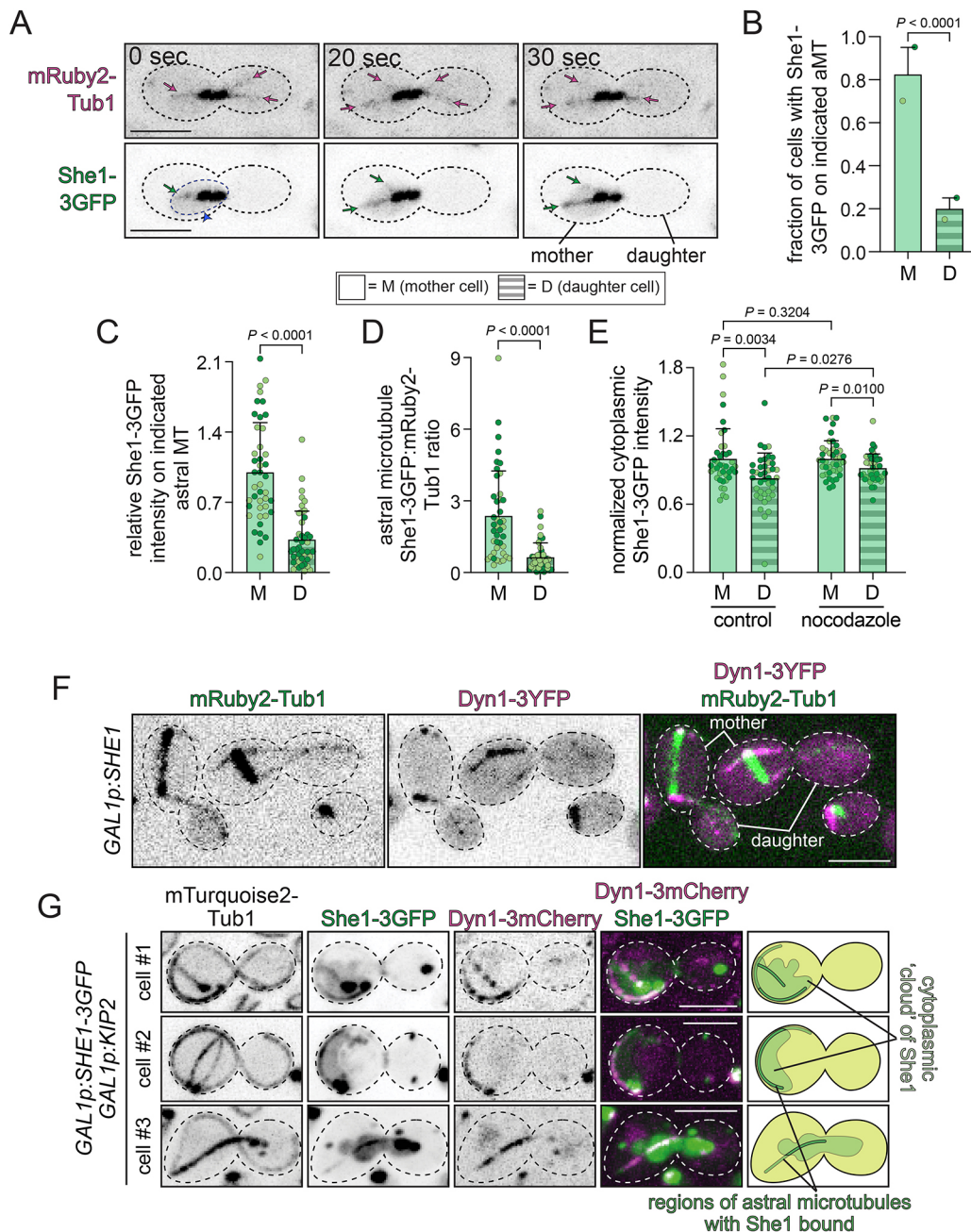


Fig. 8. She1 preferentially localizes to astral microtubules in the mother cell. (A) Representative images of an HU-arrested cell expressing mRuby2-Tub1 and overexpressing She1-3GFP. Note the presence of She1-3GFP on astral microtubules within the mother (bottom, green arrows; magenta arrows indicate astral microtubules), but not the daughter cell (blue dashed circle with arrowhead illustrates 'cloud' of dim She1 fluorescence). (B) Plot depicting the fraction of cells with apparent She1-3GFP on indicated astral microtubules (mean \pm s.d.; $n=40$ cells from two independent replicates, indicated by circles). (C,D) Plots depicting absolute astral microtubule She1-3GFP intensity values (C), or those relative to mRuby2-Tub1 (D) ($n=43$ cells from two independent replicates). For panels B–D, only cells with apparent astral microtubules in both mother and daughter cells were assessed. (E) Plot depicting cytoplasmic fluorescence intensity values for She1-3GFP from either control cells, or those treated with 100 μ M nocodazole for 30 min (which depolymerizes microtubules; see Fig. S5A and B; $n=42$ and 43 control and nocodazole-treated cells, respectively, from 2 independent replicates). For panels C–E, circles represent values from individual microtubule measurements, and bars are mean \pm s.d.. Light and dark color hues indicate data points from independent replicates. (F) Representative images showing Dyn1-3YFP localization in cells induced to overexpress She1 (also see Fig. S5C). (G) Representative images depicting Dyn1-3mCherry localization in cells induced to overexpress She1-3GFP and Kip2 (also see Fig. S5D). P -values were calculated using an unpaired two-tailed Welch's t -test, a Mann-Whitney test, or by calculating Z score (see Materials and Methods). Dashed lines in A,F,G show edges of cells. Scale bars: 4 μ m.

this was not a consequence of differences in microtubule polymer mass (e.g. microtubule bundling; Fig. 8D).

To determine whether this biased localization is a consequence of asymmetric enrichment within the cytoplasm of the mother cell or preferential microtubule-binding in this compartment, we measured

the fluorescence intensity values for regions within the cytoplasm (i.e. regions excluding microtubules) of untreated cells and those treated with the microtubule depolymerizing agent nocodazole (see Fig. S5A). This analysis revealed a small enrichment of She1-3GFP in the untreated mother cells (Fig. 8E) that was somewhat reduced in

nocodazole-treated cells. Given the large difference in microtubule-binding between the two compartments compared to these small differences in cytoplasmic intensities, these data suggest that the biased localization of She1 to mother cell-associated astral microtubules is largely achieved through differential microtubule binding activity in the two compartments.

As an alternative method to assess She1 localization, we exploited the fact that She1 overexpression leads to a relocalization of dynein from microtubule plus ends to along the length of astral microtubules as a consequence of the interaction between microtubule-bound She1 and the dynein MTBD (Ecklund et al., 2017; Markus et al., 2012b). Assessment of dynein localization in She1-overexpressing cells revealed many examples of cells with Dyn1–3YFP bound along the length of astral microtubules within the mother, but not the daughter cell (Fig. 8F; Fig. S5C).

We noted that overexpressed She1–3GFP forms diffuse ‘clouds’ of fluorescence in the vicinity of microtubules (Fig. 8A, blue arrowhead and dashed circle), suggesting that She1, and the microtubules on which it is observed, is enclosed in a membrane-bound compartment, such as the nucleus. To determine whether the She1 localization pattern described above is cytoplasmic or nuclear, we overexpressed Kip2, which leads to a substantial increase in the length of astral microtubules, and assessed the localization pattern of both She1–3GFP and Dyn1–3YFP, the latter of which is exclusively cytoplasmic (note the absence of Dyn1 from spindle regions in Fig. 8F and Fig. S5C). Although we cannot rule out that some of the diffuse She1 fluorescence is nuclear, this revealed that most of the ‘clouds’ of She1–3GFP are in fact within the cytoplasm (Fig. 8G and Fig. S5D; note the presence of She1 and dynein on long astral microtubules within the ‘clouds’). Taken together, our data reveal that She1 preferentially localizes along astral microtubules within mother cells.

DISCUSSION

Our work sheds light on the means by which She1 affects dynein activity in cells, and how it polarizes dynein-mediated spindle movements toward the daughter cell. We find that astral microtubule-bound She1 precludes the initiation of dynein-mediated spindle movements in mother cells by preventing association of dynein and dynactin with microtubule plus ends in this compartment. We also find that this requires interactions between She1 and the microtubule-bound conformation of the dynein MTBD. This activity is compartmentally specified, likely as a consequence of preferential binding of She1 to astral microtubules within mother cells. Although our prior *in vitro* work revealed the She1–dynein MTBD interaction, and demonstrated the importance of this interaction for velocity reduction in single molecule assays with purified dynein alone (Ecklund et al., 2017), the nature of in-cell inhibition of dynein activity appears to occur through an entirely distinct mechanism that is unrelated to the ability of She1 to reduce the velocity of dynein, or reduce its microtubule-dissociation rate *in vitro*. However, our new findings suggest that She1 may in fact promote microtubule interactions by active cortical Num1–dynein–dynactin complexes, similar to its effect on dynein alone in optical trapping assays. Thus, the in-cell activity of She1 appears to involve two distinct activities: (1) it precludes the initiation of dynein-mediated spindle translocation events in cells (by blocking the interaction of dynein with Pac1 and Bik1, and/or the dynein–dynactin interaction, thus limiting plus end and cortical localization), and (2) it promotes dynein–microtubule encounters subsequent to offloading and activation.

How does She1 prevent the initiation of dynein-mediated spindle movements? We find that She1 only reduces dynein events when it

can adopt the phi state (see *dyn1^{D2868K}* data), and when it is in the microtubule-bound conformational state for which She1 exhibits high affinity (compare *dyn1^{MTBD}* to *dyn1^{MTBD-HA}* cells) (Ecklund et al., 2017). Importantly, dynein does not contact the plus end directly, but rather interacts with it indirectly via Bik1 (Lammers and Markus, 2015; Sheeman et al., 2003). Thus, dynein is in a microtubule-unbound state prior to offloading to the cortex. However, we recently proposed a model whereby dynein makes direct contact with the microtubule during the offloading process, and that this contact is required to disengage dynein from the plus end-targeting machinery, thus permitting spindle translocation (Lammers and Markus, 2015). If true, this would be the first moment in the activation process when the microtubule-bound dynein MTBD encounters She1. Thus, we posit that it is at this moment when She1 somehow causes dynein to adopt the phi state (see below), which consequently breaks its contacts with Pac1 and/or dynactin (Marzo et al., 2020; Zhang et al., 2017), thus terminating the offloading event. This model is further supported by our prior observation that deletion of She1 leads to enhanced offloading of dynein to cortical sites (Markus and Lee, 2011).

How might She1–dynein MTBD binding promote the phi conformation? Although such a mechanism has not yet been described, previous studies have identified long-range allosteric communication from the MTBD to the AAA ring via the coiled-coil stalk (Kon et al., 2009; Niekamp et al., 2019; Uchimura et al., 2015), where contact points have been identified that stabilize the phi state (Marzo et al., 2020; Zhang et al., 2017). In support of such a model, we find that a dynein mutant that is less able to adopt this conformation (*Dyn1^{D2868K}*) is somewhat refractory to She1-mediated inhibition (and in fact relies on She1 for maximal in-cell activity). The same is true for Dyn1 with a C-terminal 3YFP tag, addition of which has been shown to reduce the propensity of dynein to adopt the phi conformation (Torisawa et al., 2014). Moreover, we find that She1 may prevent offloading of dynein to the mother cell cortex by reducing its plus end association, which is mediated by Pac1 (Lee et al., 2003; Sheeman et al., 2003). Our recent studies have found that Pac1 exhibits higher affinity for dynein when it is in a non-phi state (Marzo et al., 2020). Thus, reduced plus end binding may also be a consequence of She1 promoting the phi conformation.

How is She1 asymmetrically localized to the mother cell? In light of our data that She1 asymmetry is likely imparted by differential microtubule-binding affinities in the mother and daughter cells, and the likely role of phosphorylation in modulating the She1–microtubule affinity (Markus et al., 2012b), it is possible that a daughter cell-localized kinase phosphorylates She1 to reduce its microtubule binding in this compartment. Previous studies have identified the mitotic kinase Aurora B (Ipl1) and the mitogen-activated protein kinase Hog1 as candidates that phosphorylate She1 (Markus et al., 2012b; Pigula et al., 2014; Woodruff et al., 2010). At least one upstream activator of Hog1 is enriched in the daughter cell (Sho1) (Raitt et al., 2000), suggesting this kinase may be key in modulating She1 asymmetry.

Although She1 is the only known MAP that has the capacity to polarize dynein-mediated cargo transport, recent studies have revealed several MAPs in higher eukaryotes that impact motor-mediated cargo transport. For instance, MAP4 and MAP9 affect dynein–dynactin transport functions in higher eukaryotes (Monroy et al., 2020; Samora et al., 2011; Semenova et al., 2014). Of note, depletion of MAP4 leads to hyperactive cortical dynein activity and pronounced spindle movements, much like deletion of She1 (Samora et al., 2011). The mechanism by which MAP4 functions

is unclear; however, MAP9 precludes the interaction between microtubules and dynein–dynactin complexes by blocking dynactin–microtubule binding (Monroy et al., 2020). Although there is limited sequence homology among the MAP family (restricted to the microtubule-binding domains), many of them are enriched with regions of intrinsic disorder [95%, 94% and 96% of MAP9, MAP4 and She1, respectively, are predicted to be disordered according to MetaDisorder (Kozłowski and Bujnicki, 2012)]. Thus, although sequence alignments reveal no clear She1 homolog in higher eukaryotes, MAP4 and/or MAP9 may have evolved from She1, or a common ancestor.

MATERIALS AND METHODS

Plasmid generation

For expression and purification of She1–NLS^{SV40}–HaloTag, we introduced sequence encoding the nuclear localization sequence (NLS) from SV40 large T antigen (hereafter referred to as ‘NLS^{SV40}’) between She1 and the C-terminal HaloTag. Briefly, the C-terminal HaloTag sequence was PCR amplified from pProEX-HTb-TEV:*SHE1-HALO* (Markus et al., 2012b) using a forward primer that includes a sequence that encodes a short linker (Gly-Ser-Gly-Ser) followed by the NLS^{SV40} (Ala-Ala-Ala-Pro-Lys-Lys-Lys-Arg-Lys-Val-Gly). This PCR product was assembled into pProEX-HTb-TEV:*SHE1-HALO* digested with BamHI and NotI (which excises the HaloTag) using Gibson assembly, yielding pProEX-HTb-TEV:*SHE1-NLS^{SV40}-HALO*. Note this sequence (linker and NLS^{SV40}) is identical to the one introduced at the 3′ end of the *SHE1* locus to generate *she1^{NLS}*.

Media and strain construction

Strains are derived from either YEF473A or W303, and are available upon request (listed in Table S1). We transformed yeast strains using the lithium acetate method (Knop et al., 1999). Engineered yeast strains (e.g. *she1^{NLS}* and *dyn1m^{MTBD-HA}*) were constructed by PCR product-mediated transformation (Longtine et al., 1998) or by mating followed by tetrad dissection. Proper tagging and mutagenesis was confirmed by PCR and/or by sequencing. Fluorescent tubulin-expressing yeast strains were generated using plasmids and strategies described previously (Markus et al., 2015; Song and Lee, 2001). Yeast synthetic defined (SD) complete medium was obtained from Sunrise Science Products (San Diego, CA).

Live-cell imaging experiments

Assessment of cell cycle progression and spindle positioning (see Fig. 1 and Fig. S1) was performed by imaging cells in the CellASIC ONIX system using microfluidic cassettes designed for haploid yeast cells (Y04C; MilliporeSigma). In brief, after an overnight growth in SD complete medium supplemented with 2% glucose at 30°C, cells were diluted 50-fold into the cell inlet well of the microfluidic cassette, which was primed with SD complete medium prior to addition of cells (per manufacturer’s instructions). Pressure was maintained at 7.0 psi throughout the imaging period to ensure a constant replenishment of medium into the cassette, which was set to 30°C. Note that temperature is not directly monitored by the CellASIC system, and is thus affected by ambient room temperature. To account for temperature differences between experiments, wild-type and mutant cells were imaged simultaneously by introducing respective cells into adjacent imaging chambers of the microfluidics cassette. Z-stacks (7 steps with 0.5 µm spacing) from multiple XY coordinates (10 for replicate 1, and 5 for replicate 2) were acquired for 10 h at 90 s intervals. Data were normalized [$i = (x - \text{minimum value from control}) / (\text{maximum value from control} - \text{minimum value from control})$], where i is the normalized value, and x is the non-normalized value] to account for differences between independent replicates due to differences in imaging conditions (likely due to fluctuations in room temperature).

For spindle dynamics and nuclear translocation assays, mid-log phase cells were arrested with 200 mM hydroxyurea (HU) for 2.5 h in SD complete medium supplemented with 2% glucose, and then applied to slide-mounted agarose ‘pads’ consisting of 1.7% agarose dissolved in SD

complete medium supplemented with 2% glucose and 200 mM HU for confocal fluorescence microscopy. Full Z-stacks (19 planes with 0.2 µm spacing) of GFP-labeled microtubules (GFP–Tub1; for Figs 1G, 4, 5 and 6), and/or NLS-3mCherry (for Fig. 3) were acquired every 10 s for 15 min on a stage pre-warmed to 28°C. To image She1-3GFP in HU-arrested cells (for Fig. 8A–E), mid-log phase cells cultured in SD complete medium supplemented with 2% glucose were pelleted (400 g for 1 min), and then resuspended in SD complete medium supplemented with 2% galactose (to activate the *GALI* promoter). After 30 min, the cells were pelleted again, and resuspended in SD complete medium supplemented with 2% galactose and 200 mM HU for 2.5 h followed by applying them to slide-mounted agarose pads for confocal microscopy (for a total galactose induction time of 3 h). To image She1 or Dyn1 in She1- and/or Kip2-overexpressing cells (in non-HU arrested cells), cells were cultured in galactose-containing medium for 2.5 to 3 h prior to imaging. Z-stacks (7 steps with 0.6 µm spacing) of each respective channel were acquired every 20 s for 1 min. Note that to prevent bleed-through of mTurquoise2 fluorescence in the GFP channel (i.e. in cells expressing mTurquoise2–Tub1 and She1–GFP, such as in Fig. 8G) the mTurquoise2/CFP channel was acquired using a 445 laser and a CFP filter, while the GFP channel was acquired using a 514 nm laser and a YFP filter, which permits visualization of GFP, but not mTurquoise2.

Images were collected on a Nikon Ti-E microscope equipped with a 1.49 NA 100× TIRF objective, a Ti-S-E motorized stage, piezo Z-control (Physik Instrumente), an iXon DU888 cooled EM-CCD camera (Andor), a stage-top incubation system (Okolab), and a spinning disc confocal scanner unit (CSUX1; Yokogawa). 445 nm, 488 nm, 514 nm, 561 nm and 594 nm lasers housed in an LU-NV laser unit equipped with AOTF control (Nikon) were used to excite mTurquoise2, GFP, Venus, mRuby2 and mCherry, respectively, which were used with emission filters mounted in a filter wheel (ET480/40 m for mTurquoise2, ET525/50 M for GFP, ET520/40 M for Venus, and ET632/60 m for mRuby2 and mCherry; Chroma). The microscope was controlled with NIS Elements (Nikon).

For analysis of the cell cycle progression images, we used the following morphological features to define temporal landmarks in cell cycle progression: the spindle pole body duplication was identified as the first frame when two SPBs could be spatially resolved; anaphase onset was defined as the first frame when the spindle began to elongate; cytokinesis was defined as the first frame when independent movement of the spindle pole bodies was apparent (in which they moved with respect to each other, indicating complete spindle disassembly).

To assess cortical microtubule contacts and number of productive events, full Z-stacks (19 planes with 0.2 µm spacing) of GFP-labeled microtubules acquired using confocal fluorescence microscopy were converted to XY and XZ maximum intensity projections, which were both used to manually count the number of microtubule–cortex encounters, and the number of productive events (defined as those in which the spindle is observed moving coincident with a microtubule–cortex encounter). All dynein-mediated spindle movements were identified as such by the apparent directed migration of the spindle following and coincident with an astral microtubule associating with the cell cortex.

Protein purification

We purified She1–HaloTag as previously described (Ecklund et al., 2017). Briefly, *Escherichia coli* BL21 (Rosetta DE3 pLysS) cells transformed with pProEX-HTb-TEV:*SHE1-HALO* (or pProEX-HTb-TEV:*SHE1-NLS^{SV40}-HALO*) were grown at 37°C in LB supplemented with 1% glucose, 100 µg/ml carbenicillin and 34 µg/ml chloramphenicol to OD₆₀₀ 0.4–0.6, shifted to 16°C for 2 h, then induced with 0.1 mM IPTG for 14–16 h at 16°C. The cells were harvested, washed with cold water and stored at –80°C. Cells were thawed in 0.5 volume of cold 2× lysis buffer [1× buffer is 30 mM HEPES pH 7.2, 50 mM potassium acetate, 2 mM magnesium acetate, 0.2 mM EGTA, 10% glycerol, 1 mM DTT and protease inhibitor tablets (Pierce)] and then lysed by sonication (5×30 s pulses) with 1 min on ice between each pulse. The lysate was clarified at 22,000 g for 20 min, adjusted to 0.005% Triton X-100, then incubated with glutathione–agarose beads for 1 h at 4°C. The resin was then washed three times in wash buffer (30 mM HEPES pH 7.2, 50 mM potassium acetate, 2 mM magnesium

acetate, 0.2 mM EGTA, 300 mM KCl, 0.005% Triton X-100, 10% glycerol, 1 mM DTT and protease inhibitor tablets) and twice in TEV digest buffer (10 mM Tris-HCl pH 8.0, 150 mM KCl, 0.005% Triton X-100, 10% glycerol and 1 mM DTT). To fluorescently label She1-HALO, the bead-bound protein was incubated with 6.7 μ M HaloTag-TMR ligand (Promega) for 15 min at room temperature. The resin was then washed three more times in TEV digest buffer to remove unbound ligand, then incubated in TEV buffer supplemented with TEV protease for 1 h at 16°C. The resulting eluate was collected using a centrifugal filter unit (0.1 μ m, Millipore), aliquoted, drop frozen in liquid nitrogen and stored at -80°C .

Purification of ZZ-TEV-6His-GFP-3HA-GST-dynein₃₃₁-HALO (under the control of the galactose-inducible promoter *GAL1p*) was performed as previously described (Ecklund et al., 2017; Marzo et al., 2020). Briefly, yeast cultures were grown in YPA supplemented with 2% galactose, harvested, washed with cold water, and then resuspended in a small volume of water. The resuspended cell pellet was drop frozen into liquid nitrogen and then lysed in a coffee grinder (Hamilton Beach). After lysis, 0.25 volume of 4 \times lysis buffer (1 \times buffer is 30 mM HEPES pH 7.2, 50 mM potassium acetate, 2 mM magnesium acetate, 0.2 mM EGTA, 1 mM DTT, 0.1 mM Mg-ATP, 0.5 mM Pefabloc SC and 0.7 μ g/ml Pepstatin) was added, and the lysate was clarified at 22,000 *g* for 20 min. The supernatant was then bound to IgG sepharose 6 fast flow resin (Cytiva) for 1 h at 4°C, which was subsequently washed three times in wash buffer (30 mM HEPES pH 7.2, 50 mM potassium acetate, 2 mM magnesium acetate, 0.2 mM EGTA, 300 mM KCl, 0.005% Triton X-100, 10% glycerol, 1 mM DTT, 0.1 mM Mg-ATP, 0.5 mM Pefabloc SC and 0.7 μ g/ml Pepstatin), and twice in TEV buffer (50 mM Tris-HCl pH 8.0, 150 mM potassium acetate, 2 mM magnesium acetate, 1 mM EGTA, 0.005% Triton X-100, 10% glycerol, 1 mM DTT, 0.1 mM Mg-ATP, 0.5 mM Pefabloc SC). To fluorescently label 6His-GFP-GST-3HA-dynein₃₃₁-HALO (for single molecule analyses), the bead-bound protein was incubated with either 6.7 μ M HaloTag-TMR or HaloTag-PEG-biotin ligand (Promega) for 15 min at room temperature. The resin was then washed four more times in TEV digest buffer, then incubated in TEV buffer supplemented with TEV protease for 1 h. Following TEV digest, the bead solution was transferred to a spin column (Millipore) and centrifuged at 20,000 *g* for 10 s. The resulting protein solution was aliquoted, flash frozen in liquid nitrogen and then stored at -80°C .

Purification of yeast tubulin was performed essentially as described previously (Johnson et al., 2011) with minor modifications. Yeast cells (JEL1) co-transformed with p426Gal1:Tub1 and p424:Tub2-6His were grown in 50 ml of selective SD complete medium (lacking uracil and tryptophan) supplemented with 2% glucose, and then transferred to 1 l of nonselective YPGL (2% peptone, 1% yeast extract, 3% glycerol, and 2% lactate; note, we grew 16 l of cells for a typical preparation). When the cell density reached an OD₆₀₀ between 5 and 9, 20 g of galactose powder was added per liter of YPGL, and after 5 h, cells were harvested, washed with water and stored at -80°C . Approximately 75 g of cells were thawed and resuspended in 70 ml of lysis buffer (50 mM HEPES pH 7.4, 500 mM NaCl, 10 mM MgSO₄, 30 mM imidazole) supplemented with 50 μ M GTP and cComplete protease inhibitor cocktail (Roche), and lysed by 5–6 passes through a microfluidizer (LM10; Microfluidics) at 23,000 PSI, with 5 min on ice between each pass. After clarification (at 22,000 *g* for 30 min at 4°C), the supernatant was applied to a 5 ml HisTrap Ni-NTA column (Cytiva) pre-equilibrated with 10 column volumes (CVs) of lysis buffer supplemented with GTP using an AKTA FPLC (Cytiva). After washing the column with 10 CVs of lysis buffer supplemented with 50 μ M GTP and 10 CVs of nickel wash buffer (25 mM PIPES pH 6.9, 1 mM MgSO₄ and 30 mM imidazole) supplemented with 50 μ M GTP, bound protein was eluted with 6 CVs of elution buffer (25 mM PIPES pH 6.9, 1 mM MgSO₄, 300 mM imidazole) supplemented with 50 μ M GTP. Peak fractions (determined by absorbance at 260 nm) were pooled and treated with nuclease (Pierce Universal Nuclease; catalog #88702; 10 μ l per 20 ml of eluate) for 15 min at room temperature, and then diluted with MonoQ buffer A (25 mM PIPES pH 6.9, 2 mM MgSO₄, 1 mM EGTA) supplemented with 50 μ M GTP such that the final imidazole concentration was 100 mM. The protein was then loaded onto a MonoQ 10/100GL anion exchange column pre-equilibrated with 5 CVs

of 90% MonoQ buffer A (see above) and 10% MonoQ buffer B (25 mM PIPES pH 6.9, 2 mM MgSO₄, 1 mM EGTA and 1 M NaCl) supplemented with 50 μ M GTP, after which bound protein was eluted with a 10–70% MonoQ buffer B gradient over 50 CVs. Peak tubulin fractions (determined by absorbance at 260 nm and SDS-PAGE) were pooled and concentrated (Amicon Ultra-4 30K; catalog #UFC803024) to 2.8 μ M (concentration and aggregation were closely monitored using absorbance at 260 nm and 280 nm), and then dialyzed against tubulin storage buffer (10 mM PIPES pH 6.9, 1 mM MgSO₄, 1 mM EGTA) supplemented with 50 μ M GTP (Thermo Slide-A-Lyzer; catalog #66810). Resulting protein was aliquoted (50 μ l), snap frozen in liquid nitrogen and stored at -80°C .

Optical trapping

Anti-His-coated 0.44 μ m microbeads [PSS4; SpheroTech; prepared as described previously (Driver et al., 2014)] were incubated with purified 6His-GFP-3HA-GST-dynein₃₃₁-HALO in dynein trapping buffer (30 mM HEPES pH 7.2, 2 mM Mg-acetate and 1 mM EGTA) for 1 h at 4°C. During the incubation, flow chambers (assembled from a glass slide, coverslip and double-sided sticky tape) were prepared by sequential addition and incubation with the following solutions: (1) 1 mg/ml biotinylated BSA (Vector Labs #B-2007), (2) BRB80 (80 mM PIPES pH 6.9, 1 mM MgCl₂, 1 mM EGTA, pH 6.9), (3) 0.33 mg/ml Avidin (Vector Labs #A-3100), (4) BRB80, and (5) GMPCPP-stabilized biotinylated microtubules (diluted in BRB80) (Asbury et al., 2006). After a 10 min incubation, the chamber was washed with BRB80, and the dynein-coated microbeads (diluted in trapping buffer supplemented with 1 mg/ml κ -casein, 8 mg/ml BSA, 1 mM DTT, 0.8 mM ATP, 4 mM MgSO₄, 4.5 mg/ml glucose, 250 μ g/ml glucose oxidase and 30 μ g/ml catalase) were introduced into the chamber, which was then sealed with nail polish, and immediately used for data collection.

The optical trap was essentially as described previously (Franck et al., 2010), and was operated in stationary mode, without feedback control (i.e. in ‘open loop’ mode). Bead-trap separation was saved at 200 Hz and converted into force by multiplying by the trap stiffness, which ranged between 0.025 and 0.045 pN/nm. Custom analysis software written in Igor Pro (Wavemetrics; available upon request) was used to estimate pre-stall speeds, stall forces, and stall times for individual bead motility events. Briefly, we defined the start of an event as the time at which the bead first moved beyond 3 \times the root-mean-square baseline noise. The end of an event was clearly identifiable as the time when the bead detached from the microtubule. The onset of stalling was chosen as the time at which the bead velocity, averaged over a sliding 2.5-s window, first fell below 2 nm/s. Pre-stall speed was then defined as the slope of a line fit to all the data between the start of the event and the onset of stalling and stall force was defined as the average force level during the stall event.

In vitro microtubule-binding assays

We used total internal reflection fluorescence (TIRF) microscopy-based microtubule-binding assays to measure the binding affinity of She1 and She1^{NLS} for yeast microtubules. To prepare microtubules, 15 μ l of tubulin polymerization buffer (500 mM PIPES pH 6.9, 5 mM MgSO₄, 25% glycerol) along with epothilone B (50 μ M final) and GTP (2 mM final) were added to one 50 μ l aliquot of yeast tubulin (see above), which was then incubated at 30°C overnight. Flow chambers constructed from slides, double-sided sticky tape, and plasma cleaned and silanized coverslips were coated with anti-His antibody (100 μ g/ml, sc-8036, Santa Cruz Biotechnology), then blocked with 1% Pluronic F-127, after which microtubules (diluted to 0.75 μ M in tubulin polymerization buffer supplemented with 50 μ M epothilone B and 2 mM GTP) were added. After unbound microtubules were removed by washing with chamber wash buffer [a 9:1 mixture of the dynein assay buffer (30 mM HEPES pH 7.2, 50 mM potassium acetate, 2 mM magnesium acetate, 0.2 mM EGTA, 10% glycerol, supplemented with 1 mM DTT, 50 μ M epothilone B, and 2 mM GTP) and TEV buffer, as described above; this mixture was used to account for storage of purified She1-TMR in TEV buffer], purified She1-TMR (wild-type or She1^{NLS}, diluted such that the final 9:1 buffer mixture

described above was achieved for all concentrations of She1 and She1^{NLS} was introduced into the chamber. Images were collected on a Nikon Ti-E microscope (controlled with NIS Elements) equipped with a 1.49 NA 100× TIRF objective, a motorized stage, piezo Z-control (Physik Instrumente), and an iXon X3 DU897 cooled EM-CCD camera (Andor). A 561 nm laser (Coherent) was used along with a multi-pass quad filter cube set (C-TIRF for 405/488/561/638 nm; Chroma) and emission filters mounted in a filter wheel (525/50 nm, 600/50 nm, and 700/75 nm; Chroma) to image She1–TMR. To image non-fluorescent yeast microtubules, we used interference reflection microscopy (IRM), as previously described (Mahamdeh et al., 2018). Excitation light for IRM was provided by a Sola SE light engine (Lumencor). To measure the degree of She1-microtubule binding, background-subtracted fluorescence intensities of She1–TMR were determined. Note that we accounted for potential differences in the extent of HaloTag labeling between She1 and She1^{NLS} by measuring fluorescence band intensities following imaging of acrylamide gels with each on a Typhoon gel imaging system (FLA 9500). Both absolute concentration and relative degree of HaloTag labeling were taken into account when calculating binding affinities. Binding curves and curve fitting for dissociation constants (where appropriate) were generated using GraphPad Prism.

Spindle tracking and statistical analysis

Spindle tracking was performed on maximum intensity projections (XY) using a custom written MATLAB routine [available upon request; as described previously (Marzo et al., 2019)]. Dynein-mediated spindle movements were manually selected from the tracking data to obtain the various metrics described in Figs 4B–E and 5B–E. To determine the fraction of time the spindle centroid resides within 1 μm of the cell cortex (Figs 4F and 5F), an additional MATLAB routine was generated with which the user manually defines the cell cortex of the mother and bud cell. To determine the fraction of time the spindle resides within mother and daughter cell (Figs 4G and 5G), and the relative distance from the bud neck (Figs 4H and 5H), another MATLAB routine was generated in which the user manually defines the bud neck. For this latter routine, the edges of the cell were defined by cropping individual cell images such that the extreme left and right cell edges coincided with the cropped image.

Cell lysis and immunoblotting

For western blotting, yeast cultures were grown at 30°C in 3 ml SD medium supplemented with 2% glucose and harvested. Equal numbers of cells were pelleted (1500 g for 2 min) and resuspended in 0.2 ml of 0.1 M NaOH and incubated for 10 min at room temperature as described (Kushnirov, 2000). After centrifugation, the resulting cell pellet was resuspended in sample buffer and heated to 100°C for 3 min. Lysates were separated on an SDS polyacrylamide gel and electroblotted to PVDF in 25 mM Tris and 192 mM glycine supplemented with 0.05% SDS and 10% methanol for 30 min. Rabbit anti-c-Myc polyclonal (cat. no A00172, GenScript) and HRP-conjugated goat anti-rabbit-IgG antibody (Jackson ImmunoResearch Laboratories) were used at 1:1000, and 1:3000, respectively. Total protein (using Stain-Free technology; BioRad) and chemiluminescence signal were both acquired on a BioRad ChemiDoc MP gel documentation system without saturating the pixels of the camera. Band intensities (and background values) were measured using NIH ImageJ.

Statistical methods

For all datasets, *P*-values were calculated from *Z* scores (when comparing proportions) as previously described (Marzo et al., 2019), or by performing unpaired two-tailed Welch's *t*-test, or the Mann–Whitney test, the latter two of which were performed using GraphPad Prism. These latter tests were selected as follows: the unpaired two-tailed Welch's *t*-test was used when the datasets in question were both determined to be normal (by the D'Agostino and Pearson test for normality; *P*>0.05); in the case where only one (or neither) of the datasets were determined to be normal (*P*<0.05), the Mann–Whitney test was used.

Acknowledgements

We are extremely grateful to Luke Rice and members of his laboratory for sharing reagents and expertise pertaining to the expression, purification, and assembly of

yeast tubulin. We are also grateful to Jeffrey Moore for sharing the *nip100*^{ΔCAP-gly} yeast strain, and members of the Markus and DeLuca laboratories for valuable discussions.

Competing interests

The authors declare no competing or financial interests.

Author contributions

Conceptualization: K.H.E., S.M.M.; Methodology: K.H.E., M.E.B., K.A.K.; Software: C.K.D.; Validation: K.H.E., M.E.B., C.L.A.; Formal analysis: K.H.E., M.E.B., C.L.A.; Investigation: K.H.E., M.E.B., C.L.A., S.M.M.; Resources: C.L.A., S.M.M.; Data curation: K.H.E., M.E.B., K.A.K.; Writing - original draft: K.H.E., S.M.M.; Writing - review & editing: K.H.E., S.M.M.; Supervision: C.L.A., S.M.M.; Project administration: S.M.M.; Funding acquisition: C.L.A., S.M.M.

Funding

This work was funded by the NIH National Institute of General Medical Sciences (R01GM118492 and R35GM139483 to S.M.M., and R01GM079373, P01GM105537 and R35GM134842 to C.L.A.). C.L.A. was also funded by the David and Lucile Packard Foundation (fellowship 2006-30521). M.E.B. was supported by a National Institutes of Health Interdisciplinary Training Fellowship (T32CA080416). Deposited in PMC for release after 12 months.

Peer review history

The peer review history is available online at <https://journals.biologists.com/jcs/article-lookup/doi/10.1242/jcs.258510>.

References

- Adames, N. R. and Cooper, J. A. (2000). Microtubule interactions with the cell cortex causing nuclear movements in *Saccharomyces cerevisiae*. *J. Cell Biol.* **149**, 863–874. doi:10.1083/jcb.149.4.863
- Amos, L. A. (1989). Brain dynein crossbridges microtubules into bundles. *J. Cell Sci.* **93**, 19–28. doi:10.1242/jcs.93.1.19
- Asbury, C. L., Gestaut, D. R., Powers, A. F., Franck, A. D. and Davis, T. N. (2006). The Dam1 kinetochore complex harnesses microtubule dynamics to produce force and movement. *Proc. Natl. Acad. Sci. USA* **103**, 9873–9878. doi:10.1073/pnas.0602249103
- Bardin, A. J., Visintin, R. and Amon, A. (2000). A mechanism for coupling exit from mitosis to partitioning of the nucleus. *Cell* **102**, 21–31. doi:10.1016/S0092-8674(00)00007-6
- Bergman, Z. J., Xia, X., Amaro, I. A. and Huffaker, T. C. (2012). Constitutive dynein activity in She1 mutants reveals differences in microtubule attachment at the yeast spindle pole body. *Mol. Biol. Cell* **23**, 2319–2326. doi:10.1091/mbc.e12-03-0223
- Bloecher, A., Venturi, G. M. and Tatchell, K. (2000). Anaphase spindle position is monitored by the BUB2 checkpoint. *Nat. Cell Biol.* **2**, 556–558. doi:10.1038/35019601
- Caydasi, A. K., Ibrahim, B. and Pereira, G. (2010). Monitoring spindle orientation: spindle position checkpoint in charge. *Cell Div.* **5**, 28. doi:10.1186/1747-1028-5-28
- Cepeda-García, C., Delgehyr, N., Juanes Ortiz, M. A., ten Hoopen, R., Zhiteneva, A. and Segal, M. (2010). Actin-mediated delivery of astral microtubules instructs Kar9p asymmetric loading to the bud-ward spindle pole. *Mol. Biol. Cell* **21**, 2685–2695. doi:10.1091/mbc.e10-03-0197
- Chen, X., Widmer, L. A., Stangier, M. M., Steinmetz, M. O., Stelling, J. and Barral, Y. (2019). Remote control of microtubule plus-end dynamics and function from the minus-end. *eLife* **8**, e48627. doi:10.7554/eLife.48627
- Daum, J. R., Gomez-Ospina, N., Winey, M. and Burke, D. J. (2000). The spindle checkpoint of *Saccharomyces cerevisiae* responds to separable microtubule-dependent events. *Curr. Biol.* **10**, 1375–1378. doi:10.1016/S0960-9822(00)00780-6
- Denariier, E., Ecklund, K. H., Berthier, G., Favier, A., O'Toole, E. T., Gory-Faure, S., De Macedo, L., Delphin, C., Andrieux, A., Markus, S. M. et al. (2021). Modeling a disease-correlated tubulin mutation in budding yeast reveals insight into MAP-mediated dynein function. *Mol. Biol. Cell* **32**, ar10. doi:10.1091/mbc.E21-05-0237
- Dixit, R., Ross, J. L., Goldman, Y. E. and Holzbaur, E. L. (2008). Differential regulation of dynein and kinesin motor proteins by tau. *Science* **319**, 1086–1089. doi:10.1126/science.1152993
- Driver, J. W., Powers, A. F., Sarangapani, K. K., Biggins, S. and Asbury, C. L. (2014). Measuring kinetochore-microtubule interaction in vitro. *Methods Enzymol.* **540**, 321–337. doi:10.1016/B978-0-12-397924-7.00018-2
- Ecklund, K. H., Morisaki, T., Lammers, L. G., Marzo, M. G., Stasevich, T. J. and Markus, S. M. (2017). She1 affects dynein through direct interactions with the microtubule and the dynein microtubule-binding domain. *Nat. Commun.* **8**, 2151. doi:10.1038/s41467-017-02004-2

- Eshel, D., Urrestarazu, L. A., Vissers, S., Jauniaux, J. C., van Vliet-Reedijk, J. C., Planta, R. J. and Gibbons, I. R. (1993). Cytoplasmic dynein is required for normal nuclear segregation in yeast. *Proc. Natl. Acad. Sci. USA* **90**, 11172–11176. doi:10.1073/pnas.90.23.11172
- Espinet, C., de la Torre, M. A., Aldea, M. and Herrero, E. (1995). An efficient method to isolate yeast genes causing overexpression-mediated growth arrest. *Yeast* **11**, 25–32. doi:10.1002/yea.320110104
- Estrem, C., Fees, C. P. and Moore, J. K. (2017). Dynein is regulated by the stability of its microtubule track. *J. Cell Biol.* **216**, 2047–2058. doi:10.1083/jcb.201611105
- Franck, A. D., Powers, A. F., Gestaut, D. R., Davis, T. N. and Asbury, C. L. (2010). Direct physical study of kinetochore-microtubule interactions by reconstitution and interrogation with an optical force clamp. *Methods* **51**, 242–250. doi:10.1016/j.ymeth.2010.01.020
- Geiser, J. R., Schott, E. J., Kingsbury, T. J., Cole, N. B., Totis, L. J., Bhattacharyya, G., He, L. and Hoyt, M. A. (1997). *Saccharomyces cerevisiae* genes required in the absence of the CIN8-encoded spindle motor act in functionally diverse mitotic pathways. *Mol. Biol. Cell* **8**, 1035–1050. doi:10.1091/mbc.8.6.1035
- Gladfelter, A. S., Kozubowski, L., Zyla, T. R. and Lew, D. J. (2005). Interplay between septin organization, cell cycle and cell shape in yeast. *J. Cell Sci.* **118**, 1617–1628. doi:10.1242/jcs.02286
- Grava, S., Schaerer, F., Faty, M., Philippsen, P. and Barral, Y. (2006). Asymmetric recruitment of dynein to spindle poles and microtubules promotes proper spindle orientation in yeast. *Dev. Cell* **10**, 425–439. doi:10.1016/j.devcel.2006.02.018
- Greenberg, S. R., Tan, W. and Lee, W.-L. (2018). Num1 versus NuMA: insights from two functionally homologous proteins. *Biophys. Rev.* **10**, 1631–1636. doi:10.1007/s12551-018-0472-x
- Heil-Chapdelaine, R. A., Oberle, J. R. and Cooper, J. A. (2000). The cortical protein Num1p is essential for dynein-dependent interactions of microtubules with the cortex. *J. Cell Biol.* **151**, 1337–1344. doi:10.1083/jcb.151.6.1337
- Hotz, M., Leisner, C., Chen, D., Manatschal, C., Wegleiter, T., Ouellet, J., Lindstrom, D., Gottschling, D. E., Vogel, J. and Barral, Y. (2012). Spindle pole bodies exploit the mitotic exit network in metaphase to drive their age-dependent segregation. *Cell* **148**, 958–972. doi:10.1016/j.cell.2012.01.041
- Iqbal, K., Liu, F., Gong, C.-X. and Grundke-Iqbal, I. (2010). Tau in Alzheimer disease and related tauopathies. *Curr. Alzheimer Res.* **7**, 656–664. doi:10.2174/156720510793611592
- Johnson, V., Ayaz, P., Huddleston, P. and Rice, L. M. (2011). Design, overexpression, and purification of polymerization-blocked yeast α -tubulin mutants. *Biochemistry* **50**, 8636–8644. doi:10.1021/bi2005174
- Knop, M., Siegers, K., Pereira, G., Zachariae, W., Winsor, B., Nasmyth, K. and Schiebel, E. (1999). Epitope tagging of yeast genes using a PCR-based strategy: more tags and improved practical routines. *Yeast* **15**, 963–972. doi:10.1002/(SICI)1097-0061(199907)15:10B<963::AID-YEA399>3.0.CO;2-W
- Kon, T., Imamura, K., Roberts, A. J., Ohkura, R., Knight, P. J., Gibbons, I. R., Burgess, S. A. and Sutoh, K. (2009). Helix sliding in the stalk coiled coil of dynein couples ATPase and microtubule binding. *Nat. Struct. Mol. Biol.* **16**, 325–333. doi:10.1038/nsmb.1555
- Kozłowski, L. P. and Bujnicki, J. M. (2012). MetaDisorder: a meta-server for the prediction of intrinsic disorder in proteins. *BMC Bioinformatics* **13**, 111. doi:10.1186/1471-2105-13-111
- Kushnir, V. V. (2000). Rapid and reliable protein extraction from yeast. *Yeast* **16**, 857–860. doi:10.1002/1097-0061(20000630)16:9<857::AID-YEA561>3.0.CO;2-B
- Lammers, L. G. and Markus, S. M. (2015). The dynein cortical anchor Num1 activates dynein motility by relieving Pac1/LIS1-mediated inhibition. *J. Cell Biol.* **211**, 309–322. doi:10.1083/jcb.201506119
- Lee, W.-L., Oberle, J. R. and Cooper, J. A. (2003). The role of the lissencephaly protein Pac1 during nuclear migration in budding yeast. *J. Cell Biol.* **160**, 355–364. doi:10.1083/jcb.200209022
- Lee, W.-L., Kaiser, M. A. and Cooper, J. A. (2005). The offloading model for dynein function: differential function of motor subunits. *J. Cell Biol.* **168**, 201–207. doi:10.1083/jcb.200407036
- Lengefeld, J., Yen, E., Chen, X., Leary, A., Vogel, J. and Barral, Y. (2018). Spatial cues and not spindle pole maturation drive the asymmetry of astral microtubules between new and preexisting spindle poles. *Mol. Biol. Cell* **29**, 10–28. doi:10.1091/mbc.E16-10-0725
- Li, Y. Y., Yeh, E., Hays, T. and Bloom, K. (1993). Disruption of mitotic spindle orientation in a yeast dynein mutant. *Proc. Natl. Acad. Sci. USA* **90**, 10096–10100. doi:10.1073/pnas.90.21.10096
- Li, J., Lee, W.-L. and Cooper, J. A. (2005). NudEL targets dynein to microtubule ends through LIS1. *Nat. Cell Biol.* **7**, 686–690. doi:10.1038/ncb1273
- Liakopoulos, D., Kusch, J., Grava, S., Vogel, J. and Barral, Y. (2003). Asymmetric loading of Kar9 onto spindle poles and microtubules ensures proper spindle alignment. *Cell* **112**, 561–574. doi:10.1016/S0092-8674(03)00119-3
- Longtine, M. S., McKenzie, A., III, Demarini, D. J., Shah, N. G., Wach, A., Brachat, A., Philippsen, P. and Pringle, J. R. (1998). Additional modules for versatile and economical PCR-based gene deletion and modification in *Saccharomyces cerevisiae*. *Yeast* **14**, 953–961. doi:10.1002/(SICI)1097-0061(199807)14:10<953::AID-YEA293>3.0.CO;2-U
- Mahamdeh, M., Simmert, S., Luchniak, A., Schäffer, E. and Howard, J. (2018). Label-free high-speed wide-field imaging of single microtubules using interference reflection microscopy. *J. Microsc.* **272**, 60–66. doi:10.1111/jmi.12744
- Markus, S. M. and Lee, W.-L. (2011). Regulated offloading of cytoplasmic dynein from microtubule plus ends to the cortex. *Dev. Cell* **20**, 639–651. doi:10.1016/j.devcel.2011.04.011
- Markus, S. M., Punch, J. J. and Lee, W. L. (2009). Motor- and tail-dependent targeting of dynein to microtubule plus ends and the cell cortex. *Curr. Biol.* **19**, 196–205. doi:10.1016/j.cub.2008.12.047
- Markus, S. M., Plevock, K. M., St. Germain, B. J., Punch, J. J., Meaden, C. W. and Lee, W.-L. (2011). Quantitative analysis of Pac1/LIS1-mediated dynein targeting: Implications for regulation of dynein activity in budding yeast. *Cytoskeleton* **68**, 157–174. doi:10.1002/cm.20502
- Markus, S. M., Kalutkiewicz, K. A. and Lee, W.-L. (2012a). Astral microtubule asymmetry provides directional cues for spindle positioning in budding yeast. *Exp. Cell Res.* **318**, 1400–1406. doi:10.1016/j.yexcr.2012.04.006
- Markus, S. M., Kalutkiewicz, K. A. and Lee, W.-L. (2012b). She1-mediated inhibition of dynein motility along astral microtubules promotes polarized spindle movements. *Curr. Biol.* **22**, 2221–2230. doi:10.1016/j.cub.2012.10.017
- Markus, S. M., Omer, S., Baranowski, K. and Lee, W.-L. (2015). Improved plasmids for fluorescent protein tagging of microtubules in *Saccharomyces cerevisiae*. *Traffic* **16**, 773–786. doi:10.1111/tra.12276
- Marzo, M. G., Griswold, J. M., Ruff, K. M., Buchmeier, R. E., Fees, C. P. and Markus, S. M. (2019). Molecular basis for dyneinopathies reveals insight into dynein regulation and dysfunction. *eLife* **8**, e47246. doi:10.7554/eLife.47246
- Marzo, M. G., Griswold, J. M. and Markus, S. M. (2020). Pac1/LIS1 stabilizes an uninhibited conformation of dynein to coordinate its localization and activity. *Nat. Cell Biol.* **22**, 559–569. doi:10.1038/s41556-020-0492-1
- McKenney, R. J., Huynh, W., Vale, R. D. and Sirajuddin, M. (2016). Tyrosination of α -tubulin controls the initiation of processive dynein-dynactin motility. *EMBO J.* **35**, 1175–1185. doi:10.15252/embj.201593071
- Miller, R. K. and Rose, M. D. (1998). Kar9p is a novel cortical protein required for cytoplasmic microtubule orientation in yeast. *J. Cell Biol.* **140**, 377–390. doi:10.1083/jcb.140.2.377
- Monroy, B. Y., Sawyer, D. L., Ackermann, B. E., Borden, M. M., Tan, T. C. and Ori-McKenney, K. M. (2018). Competition between microtubule-associated proteins directs motor transport. *Nat. Commun.* **9**, 1487. doi:10.1038/s41467-018-03909-2
- Monroy, B. Y., Tan, T. C., Oclaman, J. M., Han, J. S., Simó, S., Niwa, S., Nowakowski, D. W., McKenney, R. J. and Ori-McKenney, K. M. (2020). A Combinatorial MAP Code Dictates Polarized Microtubule Transport. *Dev. Cell* **53**, 60–72.e4. doi:10.1016/j.devcel.2020.01.029
- Moore, J. K., D'Silva, S. and Miller, R. K. (2006). The CLIP-170 homologue Bik1p promotes the phosphorylation and asymmetric localization of Kar9p. *Mol. Biol. Cell* **17**, 178–191. doi:10.1091/mbc.e05-06-0565
- Moore, J. K., Li, J. and Cooper, J. A. (2008). Dynactin function in mitotic spindle positioning. *Traffic* **9**, 510–527. doi:10.1111/j.1600-0854.2008.00710.x
- Moore, J. K., Sept, D. and Cooper, J. A. (2009). Neurodegeneration mutations in dynactin impair dynein-dependent nuclear migration. *Proc. Natl. Acad. Sci. USA* **106**, 5147–5152. doi:10.1073/pnas.0810828106
- Niekamp, S., Coudray, N., Zhang, N., Vale, R. D. and Bhabha, G. (2019). Coupling of ATPase activity, microtubule binding, and mechanics in the dynein motor domain. *EMBO J.* **38**, e101414. doi:10.15252/embj.2018101414
- Nishida, N., Komori, Y., Takarada, O., Watanabe, A., Tamura, S., Kubo, S., Shimada, I. and Kikkawa, M. (2020). Structural basis for two-way communication between dynein and microtubules. *Nat. Commun.* **11**, 1038. doi:10.1038/s41467-020-14842-8
- Pereira, G., Höfken, T., Grindlay, J., Manson, C. and Schiebel, E. (2000). The Bub2p spindle checkpoint links nuclear migration with mitotic exit. *Mol. Cell* **6**, 1–10. doi:10.1016/S1097-2765(05)00017-1
- Pereira, G., Tanaka, T. U., Nasmyth, K. and Schiebel, E. (2001). Modes of spindle pole body inheritance and segregation of the Bfa1p-Bub2p checkpoint protein complex. *EMBO J.* **20**, 6359–6370. doi:10.1093/embj/20.22.6359
- Pigula, A., Drubin, D. G. and Barnes, G. (2014). Regulation of mitotic spindle disassembly by an environmental stress-sensing pathway in budding yeast. *Genetics* **198**, 1043–1057. doi:10.1534/genetics.114.163238
- Raitt, D. C., Posas, F. and Saito, H. (2000). Yeast Cdc42 GTPase and Ste20 PAK-like kinase regulate Sho1-dependent activation of the Hog1 MAPK pathway. *EMBO J.* **19**, 4623–4631. doi:10.1093/embj/19.17.4623
- Redwine, W. B., Hernández-López, R., Zou, S., Huang, J., Reck-Peterson, S. L. and Leschziner, A. E. (2012). Structural basis for microtubule binding and release by dynein. *Science* **337**, 1532–1536. doi:10.1126/science.1224151
- Samora, C. P., Mogessie, B., Conway, L., Ross, J. L., Straube, A. and McAnish, A. D. (2011). MAP4 and CLASP1 operate as a safety mechanism to maintain a stable spindle position in mitosis. *Nat. Cell Biol.* **13**, 1040–1050. doi:10.1038/ncb2297

- Seitz, A., Kojima, H., Oiwa, K., Mandelkow, E.-M., Song, Y.-H. and Mandelkow, E. (2002). Single-molecule investigation of the interference between kinesin, tau and MAP2c. *EMBO J.* **21**, 4896–4905. doi:10.1093/emboj/cdf503
- Semenova, I., Ikeda, K., Resaul, K., Kraikivski, P., Aguiar, M., Gygi, S., Zaliapin, I., Cowan, A. and Rodionov, V. (2014). Regulation of microtubule-based transport by MAP4. *Mol. Biol. Cell* **25**, 3119–3132. doi:10.1091/mbc.e14-01-0022
- Sheeman, B., Carvalho, P., Sagot, I., Geiser, J., Kho, D., Hoyt, M. A. and Pellman, D. (2003). Determinants of *S. cerevisiae* dynein localization and activation: implications for the mechanism of spindle positioning. *Curr. Biol.* **13**, 364–372. doi:10.1016/S0960-9822(03)00013-7
- Song, S. and Lee, K. S. (2001). A novel function of *Saccharomyces cerevisiae* CDC5 in cytokinesis. *J. Cell Biol.* **152**, 451–470. doi:10.1083/jcb.152.3.451
- Tan, R., Lam, A. J., Tan, T., Han, J., Nowakowski, D. W., Vershinin, M., Simó, S., Ori-McKenney, K. M. and McKenney, R. J. (2019). Microtubules gate tau condensation to spatially regulate microtubule functions. *Nat. Cell Biol.* **21**, 1078–1085. doi:10.1038/s41556-019-0375-5
- Torisawa, T., Ichikawa, M., Furuta, A., Saito, K., Oiwa, K., Kojima, H., Toyoshima, Y. Y. and Furuta, K. (2014). Autoinhibition and cooperative activation mechanisms of cytoplasmic dynein. *Nat. Cell Biol.* **16**, 1118–1124. doi:10.1038/ncb3048
- Trinczek, B., Ebner, A., Mandelkow, E. M. and Mandelkow, E. (1999). Tau regulates the attachment/detachment but not the speed of motors in microtubule-dependent transport of single vesicles and organelles. *J. Cell Sci.* **112**, 2355–2367. doi:10.1242/jcs.112.14.2355
- Uchimura, S., Fujii, T., Takazaki, H., Ayukawa, R., Nishikawa, Y., Minoura, I., Hachikubo, Y., Kurisu, G., Sutoh, K., Kon, T. et al. (2015). A flipped ion pair at the dynein-microtubule interface is critical for dynein motility and ATPase activation. *J. Cell Biol.* **208**, 211–222. doi:10.1083/jcb.201407039
- Vogel, J. and Snyder, M. (2000). The carboxy terminus of Tub4p is required for gamma-tubulin function in budding yeast. *J. Cell Sci.* **113**, 3871–3882. doi:10.1242/jcs.113.21.3871
- Vogel, J., Drapkin, B., Oomen, J., Beach, D., Bloom, K. and Snyder, M. (2001). Phosphorylation of γ -tubulin regulates microtubule organization in budding yeast. *Dev. Cell* **1**, 621–631. doi:10.1016/S1534-5807(01)00073-9
- Wong, J., Nakajima, Y., Westermann, S., Shang, C., Kang, J.-S., Goodner, C., Houshmand, P., Fields, S., Chan, C. S. M., Drubin, D. et al. (2007). A protein interaction map of the mitotic spindle. *Mol. Biol. Cell* **18**, 3800–3809. doi:10.1091/mbc.e07-06-0536
- Woodruff, J. B., Drubin, D. G. and Barnes, G. (2009). Dynein-driven mitotic spindle positioning restricted to anaphase by She1p inhibition of dynactin recruitment. *Mol. Biol. Cell* **20**, 3003–3011. doi:10.1091/mbc.e09-03-0186
- Woodruff, J. B., Drubin, D. G. and Barnes, G. (2010). Mitotic spindle disassembly occurs via distinct subprocesses driven by the anaphase-promoting complex, Aurora B kinase, and kinesin-8. *J. Cell Biol.* **191**, 795–808. doi:10.1083/jcb.201006028
- Yeh, E., Skibbens, R. V., Cheng, J. W., Salmon, E. D. and Bloom, K. (1995). Spindle dynamics and cell cycle regulation of dynein in the budding yeast, *Saccharomyces cerevisiae*. *J. Cell Biol.* **130**, 687–700. doi:10.1083/jcb.130.3.687
- Yeh, E., Yang, C., Chin, E., Maddox, P., Salmon, E. D., Lew, D. J. and Bloom, K. (2000). Dynamic positioning of mitotic spindles in yeast: role of microtubule motors and cortical determinants. *Mol. Biol. Cell* **11**, 3949–3961. doi:10.1091/mbc.11.11.3949
- Zhang, K., Foster, H. E., Rondelet, A., Lacey, S. E., Bahi-Buisson, N., Bird, A. W. and Carter, A. P. (2017). Cryo-EM reveals how human cytoplasmic dynein is auto-inhibited and activated. *Cell* **169**, 1303–1314.e18. doi:10.1016/j.cell.2017.05.025
- Zhu, Y., An, X., Tomaszewski, A., Hepler, P. K. and Lee, W.-L. (2017). Microtubule cross-linking activity of She1 ensures spindle stability for spindle positioning. *J. Cell Biol.* **216**, 2759–2775. doi:10.1083/jcb.201701094

Figure S1

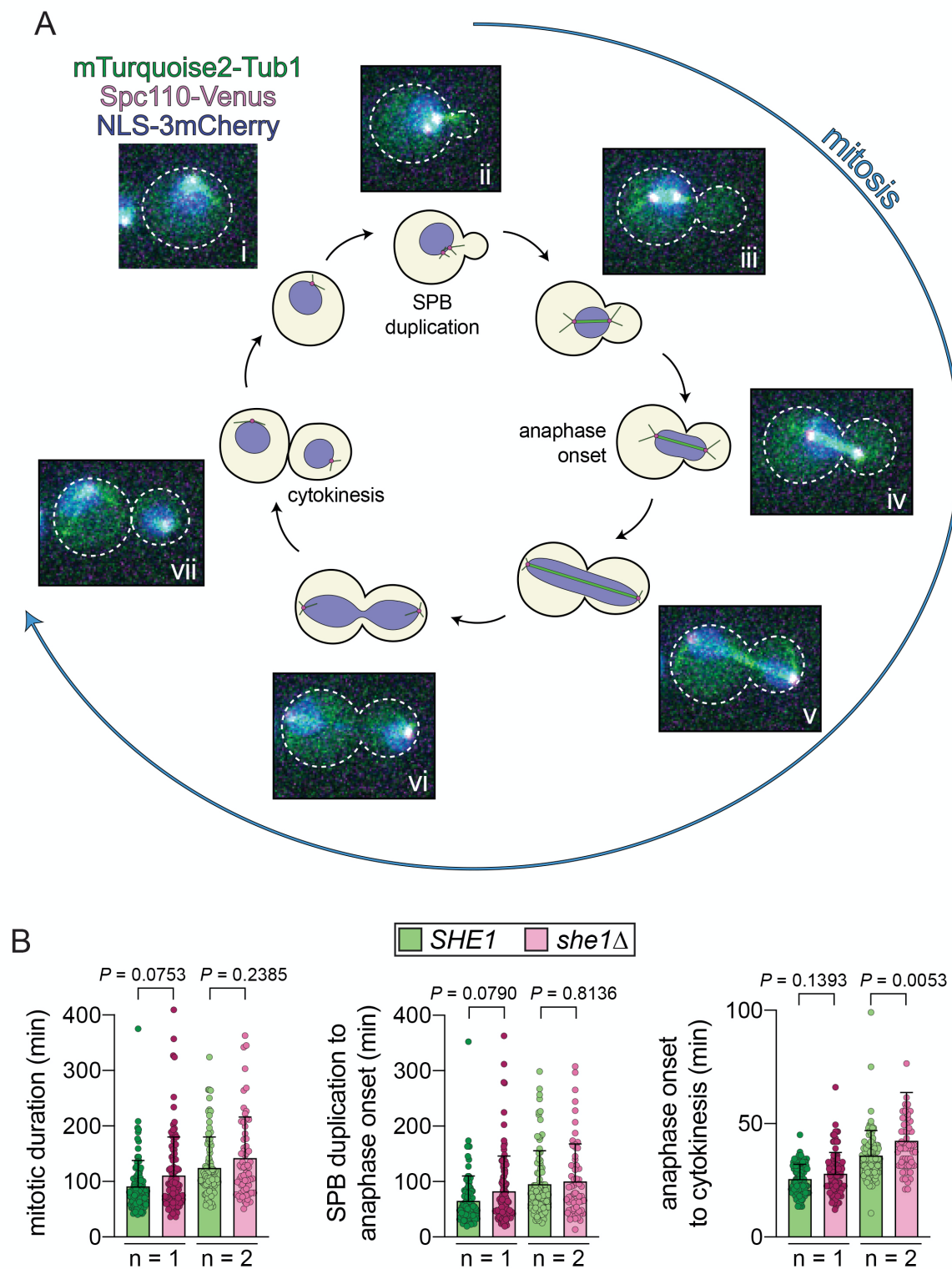


Fig. S1. Cell cycle progression analysis. (A) Representative time-lapse confocal fluorescence microscopy images of a cell expressing mTurquoise2-Tub1 (to visualize microtubules), Spc110-Venus (to visualize spindle pole bodies, or SPBs), and NLS-3mCherry (to visualize the nucleus). Cells were grown in a microfluidics cassette (CellAsic ONIX; see Methods), and imaged over the course of several cell cycles. (B) Plots depicting absolute time intervals between indicated temporal landmarks for independent replicates 1 and 2 (see Figure 1 for normalized data, and n values). Images for independent replicates for *SHE1* and *she1* Δ cells were acquired simultaneously (*i.e.*, *SHE1* and *she1* Δ replicate #1 were acquired together; see Methods) to account for potential differences in room temperature.

Figure S2

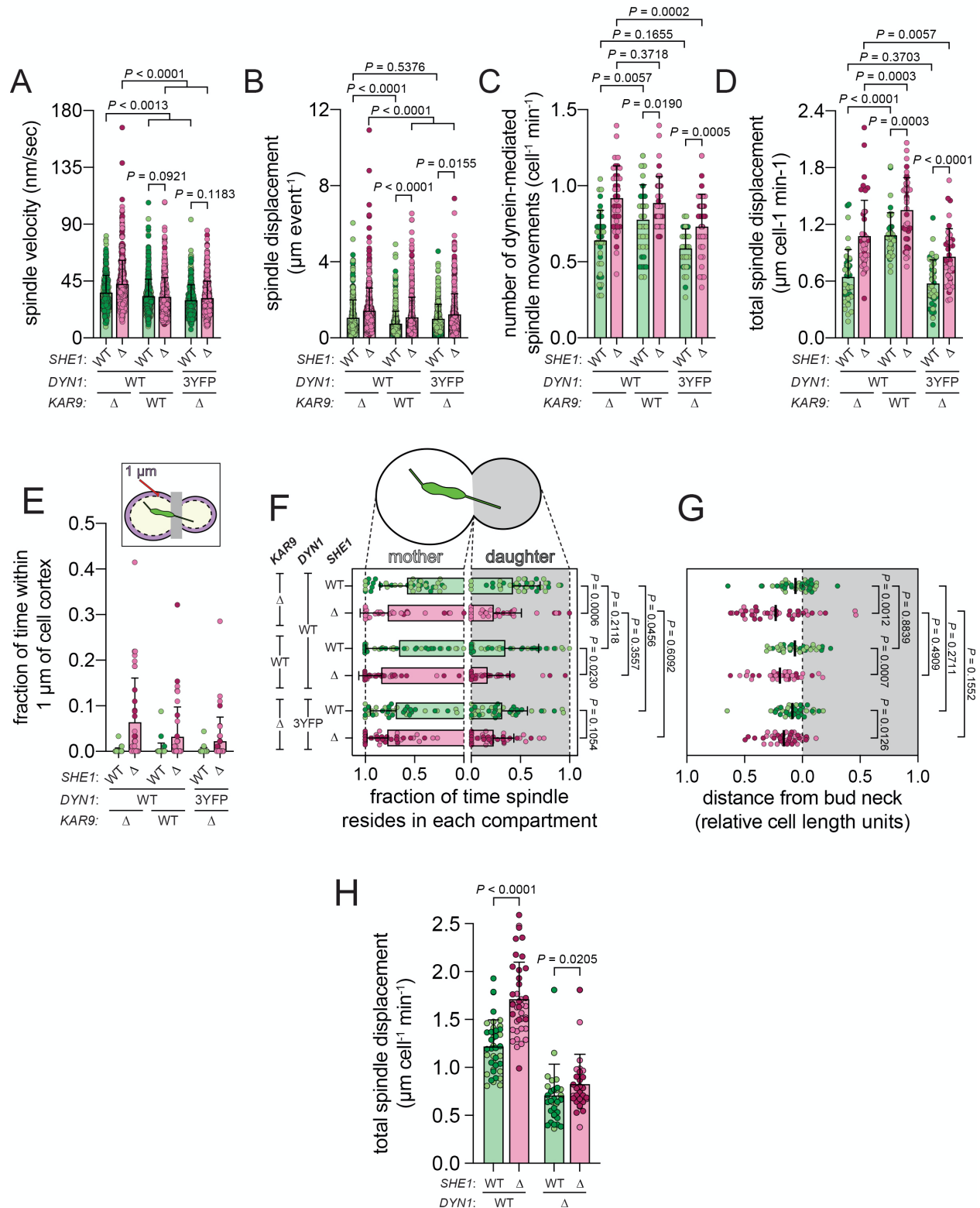


Fig. S2. Effects of *KAR9* and the 3YFP tag on dynein-mediated spindle

movements. (A – D) Dynein-mediated spindle movements were manually selected from the tracking data, from which velocity (A), displacement (B, per event; or, C, per minute), and the number of dynein-mediated spindle movements per minute (D) were obtained (mean \pm standard deviation is overlaid with scatter plot of all data points). See Figures 4 and 5 for *n* values for all *kar9* Δ data points; for *KAR9 SHE1* and *KAR9 she1* Δ , *n* = 459 (40), and 448 (40) spindle movement events (number of cells), respectively, from 2 independent replicates). (E - G) The fraction of spindle coordinates that reside within 1 μ m of the cell cortex (E; mean \pm standard deviation overlaid with data from individual cells), or within the mother and daughter cell are plotted (F; circles represent data for individual cells). (G) The mean position of the spindle centroid (along the longitudinal mother-daughter axis only) for each cell (circles represent mean spindle position for individual cells over the course of a 15 minute movie, and lines indicate mean values for all cells). See Figures 4 and 5 for *n* values for all *kar9* Δ data points; for *KAR9 SHE1* and *KAR9 she1* Δ , *n* = 40 cells for each. *P* values were calculated using either the Mann-Whitney or an unpaired two-tailed Welch's *t*-test (see Methods; also see Figures 4 and 5 for *P* values comparing *SHE1* datasets to those from *she1* Δ cells). For all panels, light and dark color hues indicate data points from independent replicates. (H) Plots depicting total spindle displacement per minute for indicated yeast strains (from all tracking data, not just dynein-mediated displacement; from left to right, *n* = 40, 40, 35 and 35 cells from 2 independent replicates) .

Figure S3

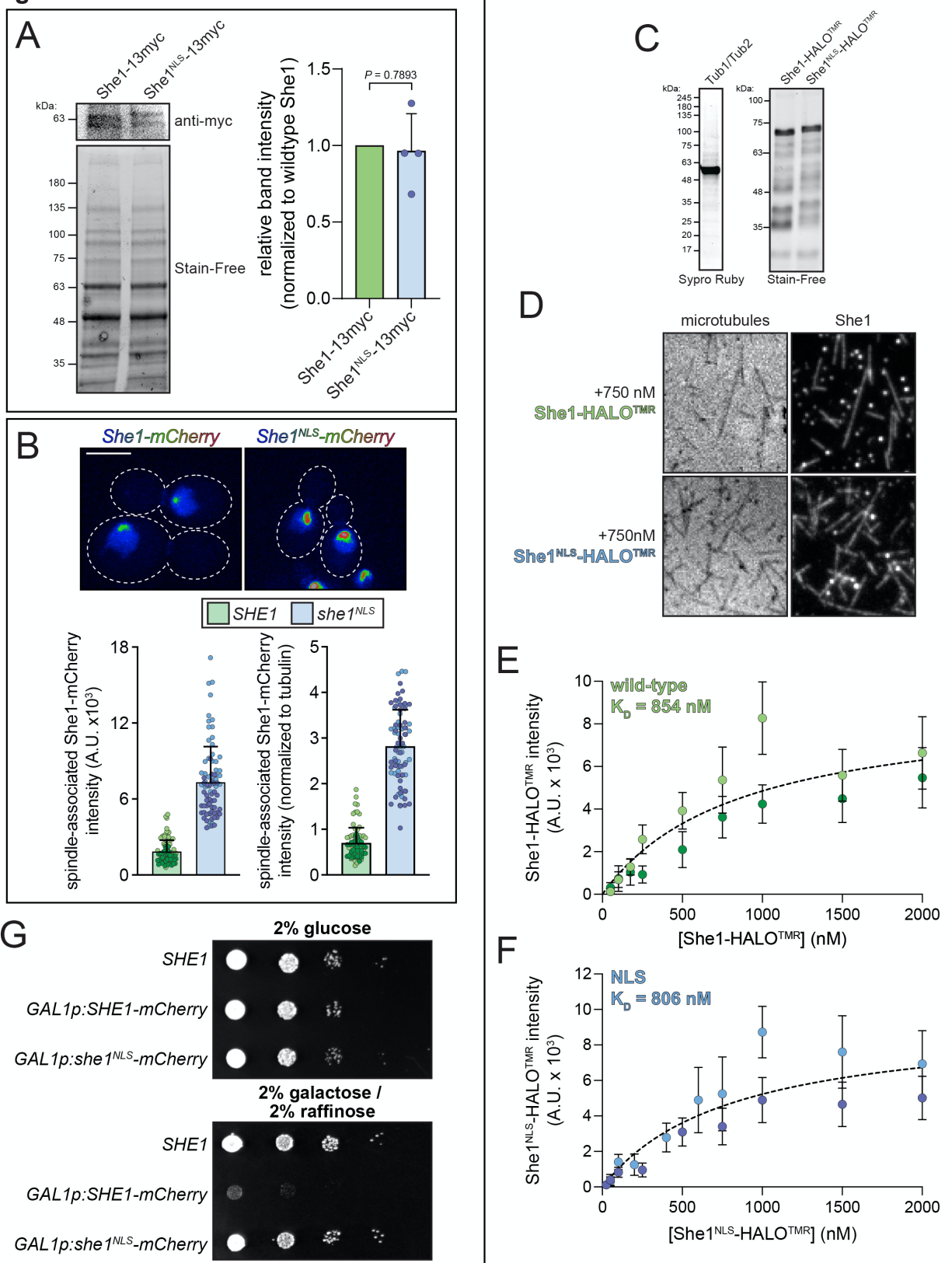


Fig. S3. Characterization of She1^{NLS}. (A) Representative immunoblot (top) and Stain-Free image (bottom) of extracts prepared from cells expressing She1-13myc (wild-type or She1^{NLS}) and separated by SDS PAGE. Total protein was imaged using Stain-Free technology (BioRad; bottom), and used as a loading control. Background-subtracted band intensities (corrected for differences in sample loading) for She1^{NLS}-13myc from each replicate (n = 2 independent experiments, with 2 lysate concentrations per immunoblot) were directly compared to that from each respective wild-type, which was normalized to 1. (B) Representative images (shown as a colormap) and plots depicting fluorescence intensity values (and those normalized to spindle-localized GFP-Tub1) of spindle localized She1- or She1^{NLS}-mCherry (overexpressed for 3 hours). (C) Recombinant proteins used in binding assays (left, alpha/beta-tubulin from yeast; right, She1 proteins from bacteria). (D) Representative images of microtubule-bound She1 (wild-type and She1^{NLS}) used in quantitation of binding affinities. (E and F) Plots depicting relative microtubule binding of wild-type (E) and She1^{NLS} (F) as a function of concentration (open and closed circles represent values obtained from independent replicates; n = 2). Background subtracted intensity values for microtubule-bound She1 were plotted against concentration, and the data were fit (using GraphPad Prism) to obtain K_D values, as shown. (G) Serial dilutions of cells with the indicated genotype grown on YPA media supplemented with either 2% glucose, or 2% glucose/2% raffinose. Note that addition of the NLS to She1 eliminates growth defects apparent in cells overexpressing wild-type She1.

Figure S4

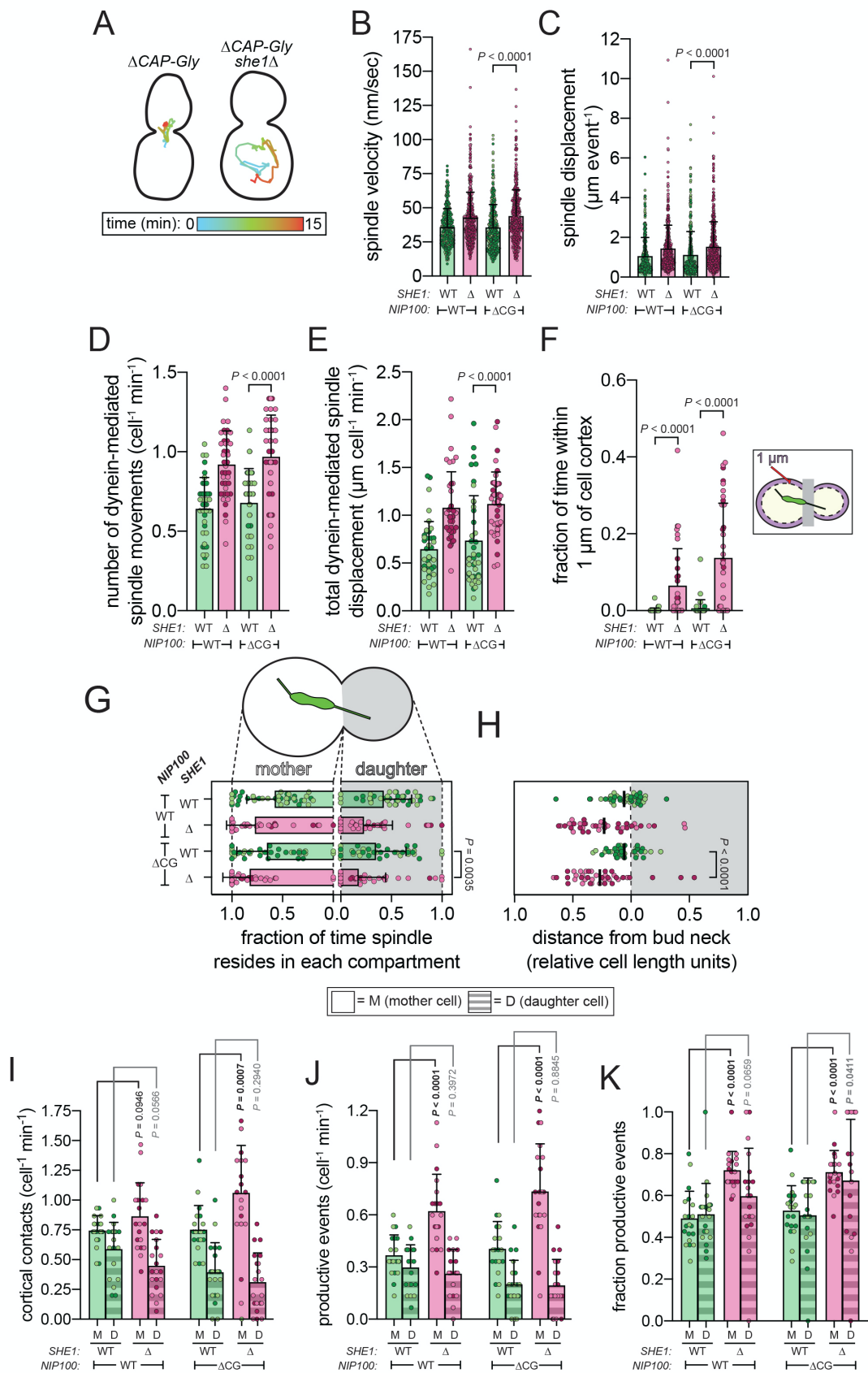


Fig. S4. Removal of the Nip100 CAP-Gly domain has no effect on dynein-mediated spindle movements, nor She1 activity. (A) Representative spindle tracks from indicated strains. Hydroxyurea-arrested *kar9Δ* cells (along with indicated genotype) expressing GFP-Tub1 were imaged, and the centroid of the spindle was tracked over time (see Fig. 4A). (B – E) Plots depicting (B) velocity, (C) displacement (per event), (D) and number and (E) extent (displacement per minute) of dynein-mediated spindle movements (mean ± standard deviation, overlaid with all data points; from left to right, n = 315 (40), 448 (40), 391 (40), and 440 (40) spindle movement events (number of cells) from 2 independent replicates). (F and G) The fraction of spindle coordinates that reside within 1 μm of the cell cortex (F; mean ± standard deviation overlaid with data from individual cells) or within the mother and daughter cell are plotted (G; circles represent data for individual cells). (H) The mean longitudinal position of the spindle centroid for each cell (circles represent data for individual cells). For panels F – H, from left to right (or top to bottom for G and H) n = 40 cells for each from 2 independent replicates. For all panels, light and dark color hues indicate data points from independent replicates (“ΔCG”, *nip100^{ΔCAP-gly}*). (I) The numbers of astral microtubule plus end-cortex encounters (I) and of ‘productive’ dynein-mediated spindle translocation events (J) are plotted, as well as the fraction of cortical contacts that convert to a productive event (K; for all strains, n = 20 cells from 2 independent replicates). All *P* values were calculated using either the Mann-Whitney or an unpaired two-tailed Welch’s *t*-test. For all panels, light and dark color hues indicate data points from independent replicates.

Figure S5

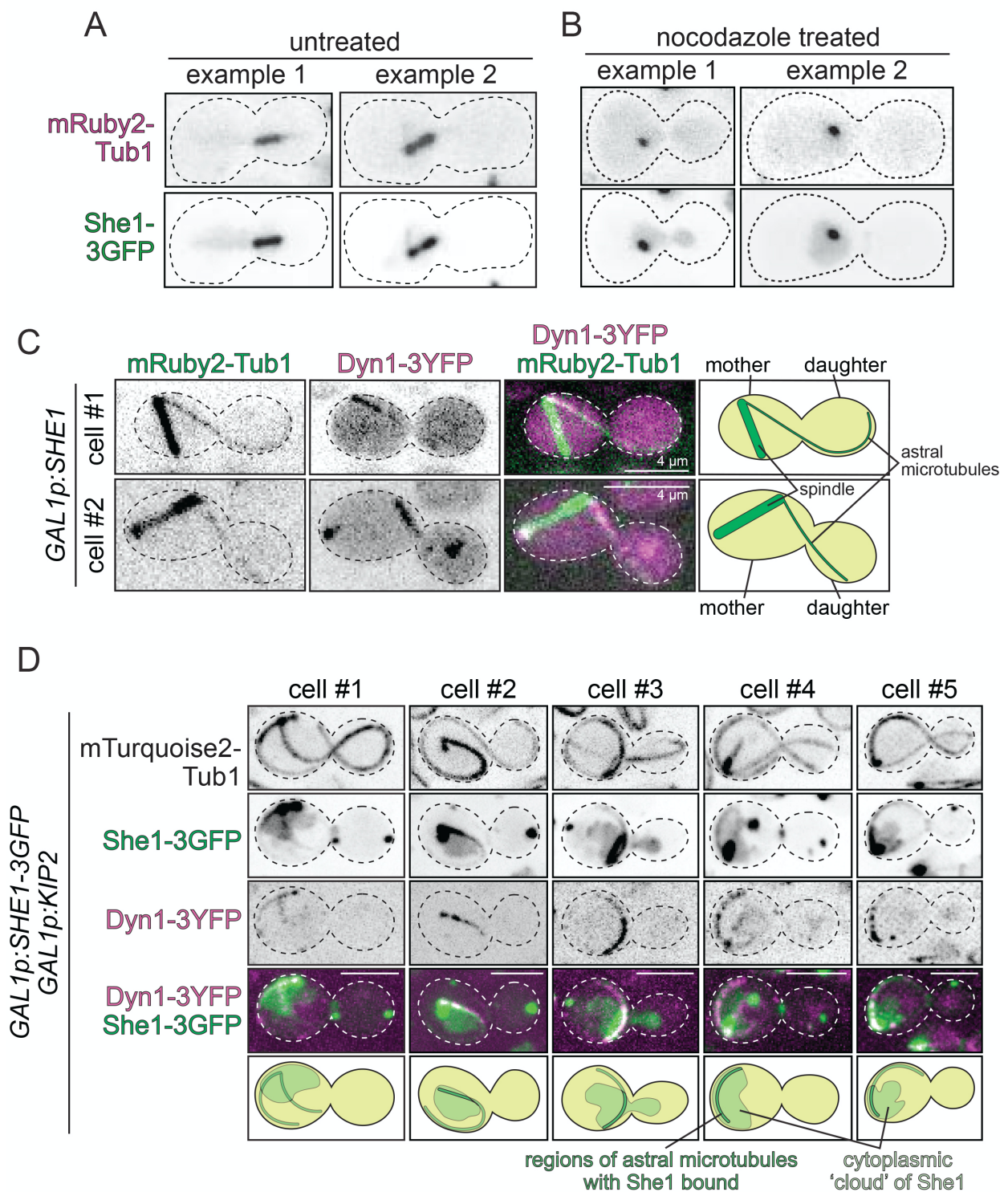


Fig. S5. Additional assessment of She1 localization in cells. (A and B)

Representative microscopy images of hydroxyurea-arrested cells expressing mRuby2-Tub1 and overexpressing She1-3GFP (as described in Figure 8) showing that nocodazole eliminates microtubules. Those in panels A and B are examples of untreated cells, and those treated with 100 μ M nocodazole for 30 minutes prior to imaging, respectively. Note the absence of clear microtubule-based structures (astral and spindle microtubules). However, we noted the appearance of bright spots in both mRuby2-Tub1 and She1-3GFP channels upon nocodazole treatment, which may be a collapsed spindle and/or single SPB with very short microtubules to which She1 could bind. (C) Additional examples showing that overexpression of She1 (by growth in galactose-containing media for 2.5 hours) leads to relocalization of dynein from plus ends to along the length of the astral microtubule within the mother, but not the daughter cells, indicating that She1 is also enriched on these microtubule regions. (D) Additional examples showing the localization of Dyn1-3mCherry in cells induced to overexpress She1-3GFP and Kip2 for 3 hours. Note the colocalization of She1 and Dyn1 along microtubules within the mother, but not the daughter, indicating that She1 indeed preferentially localizes to astral microtubules within the mother. Also note that the ‘clouds’ of She1-3GFP fluorescence were almost always within the vicinity of astral microtubules, indicating this fluorescence is not necessarily nuclear (as apparent from the Dyn1-3mCherry localization pattern).

Table S1. List of yeast strains used throughout the study.

Strain	Genotype	Background	Source
120	Mata <i>GFP-TUB1::LEU2 ura3-52 lys2-801 leu2-Δ1 his3-Δ200 trp1-Δ63</i>	YEF473	This study
191	Mata <i>she1Δ::KAN^R GFP-TUB1::LEU2 ura3-52 lys2-801 leu2-Δ1 his3-Δ200 trp1-Δ63</i>	YEF473	This study
193	Mata <i>kar9Δ::KAN^R GFP-TUB1::LEU2 ura3-52 lys2-801 leu2-Δ1 his3-Δ200 trp1-Δ63</i>	YEF473	This study
627	Mata <i>dyn1^{mMTBD}-3YFP::TRP kar9Δ::KAN^R she1Δ::HIS3 GFP-TUB1::LEU2 ura3-52 lys2-801 leu2-Δ1 his3-Δ200 trp1-Δ63</i>	YEF473	This study
714	Mata <i>dyn1^{mMTBD}-3YFP::TRP kar9Δ::KAN^R GFP-TUB1::LEU2 ura3-52 lys2-801 leu2-Δ1 his3-Δ200 trp1-Δ63</i>	YEF473	This study
818	Mata <i>bni1Δ::TRP1 MYO1-EGFP::HPH NUP133-3mCherry::URA3 ura3-52 lys2-801 leu2-Δ1 his3-Δ200 trp1-Δ63</i>	YEF473	This study
820	Mata <i>MYO1-EGFP::HPH NUP133-3mCherry::URA3 ura3-52 lys2-801 leu2-Δ1 his3-Δ200 trp1-Δ63</i>	YEF473	This study
1008	Mata <i>GAL1p:ZZ-TEV-6xHis-GFP-3XHA-GST-dyn1³³¹-HALO::KAN^R prb1Δ his3-11,15 ura3-52 leu2-3,112 ade2-1 trp-1 pep4Δ::HIS5</i>	W303	(Ecklund et al., 2017)
1437	Mata <i>she1Δ::URA3 kar9Δ::KAN^R GFP-TUB1::LEU2 ura3-52 lys2-801 leu2-Δ1 his3-Δ200 trp1-Δ63</i>	YEF473	This study
1453	Mata <i>kar9Δ::KAN^R she1^{NLS}::TRP1 GFP-TUB1::LEU2 ura3-52 lys2-801 leu2-Δ1 his3-Δ200 trp1-Δ63</i>	YEF473	This study
1568	Mata <i>kar9Δ::KAN^R she1Δ::HIS3 bni1Δ::TRP1 ura3-52::TEF1p:NLS^{SV40}-3mCherry::URA3 GFP-TUB1::LEU2 lys2-801 leu2-Δ1 his3-Δ200 trp1-Δ63</i>	YEF473	This study
1569	Mata <i>kar9Δ::KAN^R she1Δ::HIS3 ura3-52::TEF1p:NLS^{SV40}-3mCherry::URA3 GFP-TUB1::LEU2 lys2-801 leu2-Δ1 his3-Δ200 trp1-Δ63</i>	YEF473	This study
1570	Mata <i>kar9Δ::KAN^R ura3-52::TEF1p:NLS^{SV40}-3mCherry::URA3 GFP-TUB1::LEU2 lys2-801 leu2-Δ1 his3-Δ200 trp1-Δ63</i>	YEF473	This study
1606	Mata <i>kar9Δ::KAN^R bni1Δ::TRP1 ura3-52::TEF1p:NLS^{SV40}-3mCherry::URA3 GFP-TUB1::LEU2 lys2-801 leu2-Δ1 his3-Δ200 trp1-Δ63</i>	YEF473	This study
1855	Mata <i>leu2 trp1 ura3-52 prb1-1122 pep4-3 Δhis3::PGAL10-GAL4</i>	JEL1	provided by Luke Rice at UT Southwestern

2029	Mata <i>kar9Δ::KAN^R she1Δ::URA3 nip100^{ΔCAP-Gly} GFP-TUB1::LEU2 ura3-52 lys2-801 his3-Δ200 trp1-Δ63</i>	YEF473	This study
2053	Mata <i>kar9Δ::KAN^R dyn1^{D2868K}-3GFP::TRP1 GFP-TUB1::LEU2 ura3-52 lys2-801 leu2-Δ1 his3-Δ200 trp1-Δ63</i>	YEF473	This study
2066	Mata <i>kar9Δ::KAN^R nip100^{ΔCAP-Gly} GFP-TUB1::LEU2 ura3-52 lys2-801 leu2-Δ1 his3-Δ200 trp1-Δ63</i>	YEF473	This study
2077	Mata <i>SPC110-Venus::LEU2 ura3-52::NLS^{SV40}-3mCherry::URA3 TUB1+3'UTR::HPH::HIS3p:mTurquoise-TUB1 lys2-801 leu2-Δ1 his3-Δ200 trp1-Δ63</i>	YEF473	This study
2078	Mata <i>she1Δ::HIS3 SPC110-Venus::LEU2 TUB1+3'UTR::HPH::HIS3p:mTurquoise-TUB1 ura3-52::NLS^{SV40}-3mCherry::URA3 lys2-801 leu2-Δ1 his3-Δ200 trp1-Δ63</i>	YEF473	This study
2192	Mata <i>tub1^{G437R}+3'UTR::HPH::HIS3p:EGFP-tub1^{G437R}+135nt of 3'UTR::HIS3 kar9Δ::KAN^R ura3-52 lys2-801 leu2-Δ1 his3-Δ200 trp1-Δ63</i>	YEF473	This study
2194	Mata <i>tub1^{G437R}+3'UTR::HPH::HIS3p:EGFP-tub1^{G437R}+135nt of 3'UTR::HIS3 she1Δ::URA3 kar9Δ::KAN^R ura3-52 lys2-801 leu2-Δ1 his3-Δ200 trp1-Δ63</i>	YEF473	This study
2223	Mata <i>dyn1^{mMTBD-HA}-3YFP::TRP1 GFP-TUB1::LEU2 kar9Δ::KAN^R she1Δ::HIS3 ura3-52 lys2-801 leu2-Δ1 his3-Δ200 trp1-Δ63</i>	YEF473	This study
2224	Mata <i>dyn1^{mMTBD-HA}-3YFP::TRP1 GFP-TUB1::LEU2 kar9Δ::KAN^R ura3-52 lys2-801 leu2-Δ1 his3-Δ200 trp1-Δ63</i>	YEF473	This study
2297	Mata <i>kar9Δ::KAN^R GFP-TUB1::LEU2 DYN1-3YFP::TRP1 ura3-52 lys2-801 leu2-Δ1 his3-Δ200 trp1-Δ63</i>	YEF473	This study
2303	Mata <i>dyn1Δ::TRP1 kar9Δ::KAN^R she1Δ::HIS3 ura3-52::TEF1p:NLS^{SV40}-3mCherry::URA3 GFP-TUB1::LEU2 lys2-801 leu2-Δ1 his3-Δ200 trp1-Δ63</i>	YEF473	This study
2304	Mata <i>GFP-TUB1::LEU2 dyn1Δ::TRP1 kar9Δ::KAN^R ura3-52::TEF1p:NLS^{SV40}-3mCherry::URA3 lys2-801 leu2-Δ1 his3-Δ200 trp1-Δ63</i>	YEF473	This study
2318	Mata <i>kar9Δ::KAN^R DYN1-3YFP::TRP1 she1Δ::HIS3 GFP-TUB1::LEU2 ura3-52 lys2-801 leu2-Δ1 his3-Δ200 trp1-Δ63</i>	YEF473	This study

2431	Mata <i>KAN^R::GAL1p:SHE1-3GFP::TRP1 TUB1+3'UTR::HPH::HIS3p:mRuby2-TUB1 ura3-52 lys2-801 leu2-Δ1 his3-Δ200 trp1-Δ63</i>	YEF473	This study
2535	Mata <i>kar9Δ::KAN^R she1Δ::URA3 dyn1^{D2868K}- 3GFP::TRP1 GFP-TUB1::LEU2 ura3-52 lys2-801 leu2- Δ1 his3-Δ200 trp1-Δ63</i>	YEF473	This study
2909	Mata <i>SHE1-13Myc::HPH::TRP1 kar9Δ::KAN^R GFP- TUB1::LEU2 ura3-52 lys2-801 leu2-Δ1 his3-Δ200 trp1- Δ63</i>	YEF473	This study
3009	Mata <i>she1^{NLS}-13Myc::HPH::TRP1 kar9Δ::KAN^R GFP- TUB1::LEU2 ura3-52 lys2-801 leu2-Δ1 his3-Δ200 trp1- Δ63</i>	YEF473	This study
3232	Mata <i>KAN^R::GAL1p:She1^{NLS}-mCherry::HIS3 GFP- TUB1::LEU2 ura3-52 lys2-801 leu2-Δ1 his3-Δ200 trp1- Δ63</i>	YEF473	This study
3238	Mata <i>KAN^R::GAL1p:She1-mCherry::HIS3 GFP- TUB1::LEU2 ura3-52 lys2-801 leu2-Δ1 his3-Δ200 trp1- Δ63</i>	YEF473	This study
3354	Mata <i>KAN^R::GAL1p:She1-3GFP::TRP1 KAN^R::GAL1p:KIP2 DYN1-3mCherry::HIS3 TUB1+3'UTR::HPH::HIS3p:mTurquoise-TUB1 ura3-52 lys2-801 leu2-Δ1 his3-Δ200 trp1-Δ63</i>	YEF473	This study

**dyn1m^{MTBD}* is a mutant *DYN1* with the microtubule binding domain (MTBD; residues 3102-3225) replaced with the corresponding region from mouse dynein (residues 3284-3407) (Ecklund et al., 2017).

***dyn1^{mMTBD-HA}* is the same, but with E3289K and E3378K, which increases affinity of the MTBD for microtubules (Redwine et al., 2012).